



HAL
open science

Investigation of fracture source mechanisms through full-field imaging and acoustic emission

Raphael Heinzmann, Rian Seghir, Syed Yasir Alam, Julien Réthoré

► **To cite this version:**

Raphael Heinzmann, Rian Seghir, Syed Yasir Alam, Julien Réthoré. Investigation of fracture source mechanisms through full-field imaging and acoustic emission. *Engineering Fracture Mechanics*, 2023, 295, pp.109744. 10.1016/j.engfracmech.2023.109744 . hal-04149446v2

HAL Id: hal-04149446

<https://hal.science/hal-04149446v2>

Submitted on 21 Nov 2023

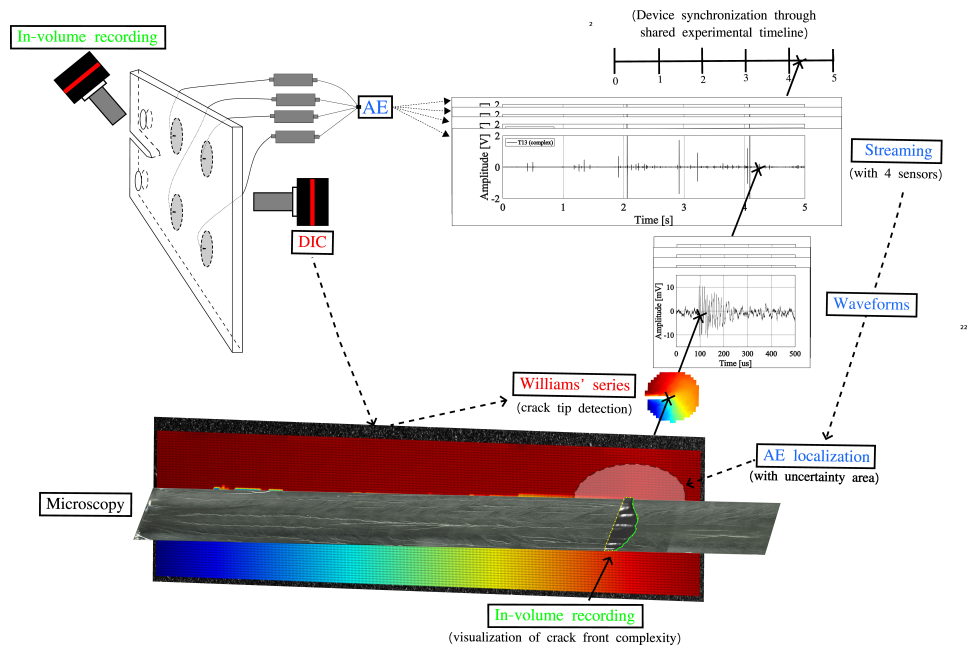
HAL is a multi-disciplinary open access archive for the deposit and dissemination of scientific research documents, whether they are published or not. The documents may come from teaching and research institutions in France or abroad, or from public or private research centers.

L'archive ouverte pluridisciplinaire **HAL**, est destinée au dépôt et à la diffusion de documents scientifiques de niveau recherche, publiés ou non, émanant des établissements d'enseignement et de recherche français ou étrangers, des laboratoires publics ou privés.

1 Graphical Abstract

2 Investigation of fracture source mechanisms through full-field imaging and
3 acoustic emission

4 Raphael Heinzmann, Rian Seghir, Syed Yasir Alam, Julien Réthoré



5 Highlights

6 **Investigation of fracture source mechanisms through full-field imaging and**
7 **acoustic emission**

8 Raphael Heinzmann, Rian Seghir, Syed Yasir Alam, Julien Réthoré

- 9 • Combining time resolved AE, DIC and in-volume measurements with
10 post-mortem fracture surface analysis on transparent PMMA tensile
11 cracking experiments. Tools applied for the purpose of AE localization,
12 crack tip detection and determination of crack front complexities and
13 kinematics within the volume, respectively.
- 14 • AE sources and the crack front can undoubtedly be connected for AE sig-
15 nals with high amplitudes such as dynamic instabilities.
- 16 • Classification of lower amplitude signals remains difficult to connect un-
17 ambiguously to a particular source mechanism even for highly correlated
18 waveforms.

19 Investigation of fracture source mechanisms through
20 full-field imaging and acoustic emission

21 Raphael Heinzmann^a, Rian Seghir^a, Syed Yasir Alam^a, Julien Réthoré^a

^a*Nantes Université, Ecole Centrale Nantes, CNRS, GeM, UMR 6183, Nantes, F-44000, , France*

22 **Abstract**

The identification and understanding of fracture processes is a vital component in securing engineering structures. By collecting data through experiments or simulations, the identification of material parameters and the understanding of failure mechanisms can be investigated. In the context of in-laboratory experiments, this is done by provoking fracture process through destructive testing (TD) techniques, while collecting data by non-destructive testing (NDT) techniques and postmortem analysis. While NDT techniques are often used individually, increasing interest is given to collective investigations of source activities. Like this, limitations of one method can be compensated by the next. A multi-modal experimental setup is proposed for holistic understanding of source mechanisms. Combined time resolved AE, DIC and in-volume measurements with post-mortem fracture surface analysis are applied on PMMA tensile cracking experiments for the purpose of AE localization, crack tip detection and determination of crack front complexities and kinematics, respectively. Both high and lower amplitude AE signals were captured and respectively associated to localized dynamic instabilities and stable crack advance. Signals are analysed individually using localization, waveform analysis, and AE descriptor classification. Crack front velocity heterogeneities are identified as valuable quantity to correlate with fracture induced AE responses. For dynamic instabilities, a linear relationship between AE absolute energy and crack propagation area was found. While identification and analyses of local and global dynamic instabilities has shown to be rather trivial, difficulties arose with respect to quasi-static related AE events.

23 **Keywords:** Polymers, Fracture Mechanics, DIC, AE, Source Localization

24 **1. Introduction**

25 To improve the security of engineering structures, one needs to identify
26 and understand different failure sources. The understanding of fracture be-
27 haviours, their initiation and propagation, is vital in the field of mechanical en-
28 gineering. With the aim of collecting experimental data to support the under-
29 standing through simulations, different fracture processes are provoked in lab-
30 oratories by destructive testing (DT) techniques (e.g. fatigue, tensile (elonga-
31 tion) or torsion experiments), with non-destructive testing (NDT) techniques
32 monitoring the activity. Classical experimental setups present an individual
33 application of NDT methods for data collection. However, combining differ-
34 ent NDT methods can provide a more robust and adequate understanding of
35 the phenomenon of interest, due to the particular set of advantages and limi-
36 tations of each NDT technique (Wang et al., 2020; Kong et al., 2020).

37 One commonly used technique is the method of Acoustic Emissions (AE).
38 With the material being subjected to external loads, sudden stress redistribu-
39 tion take place in the material due to permanent or irreversible damage phe-
40 nomena. This causes the release of elastic strain energy in the form of dissipa-
41 ted heat and elastic waves. The transient elastic waves, as surface motion,
42 are captured by a transducer translating the mechanical to electrical energy
43 through the process of piezoelectricity (Arnau and Soares, 2008). After pre-
44 amplification, electrical signals are interpreted and used for the investigation
45 of source activities. Globally, AE analysis can be subdivided into three branches
46 of application: localization, lifetime prediction and damage analysis. The aim
47 of this work is however solely related to AE as a technique for damage analy-
48 sis, where AE signals have shown to be highly dependent on the type of source
49 mechanism. In literature, AE has been shown to be applicable to different ma-
50 terials – e.g. CFRP laminates (Andraju and Raju, 2023), carbon/glass fiber re-
51 inforced composites (Gul et al., 2021), mild steel (Shrama et al., 2015), or con-
52 crete (Aggelis, 2011) – and to be sensitive to different physical or chemical phe-
53 nomena – material degradation (e.g. cracking (Kong et al., 2020)), reversible
54 processes (e.g. melting or solidification (Wadley and Mehrabian, 1984)), fabri-
55 cation processes (e.g. grinding (Jayakumar et al., 2005)), leak and flow (e.g. gas
56 evolution (Cao et al., 1998)) – as potential source mechanisms. The appear-
57 ance of these source activities are generally identified – supported by meth-
58 ods like machine learning (Almeida et al., 2023; Ciaburro and Iannace, 2022),
59 parameter clustering analysis (Li et al., 2014) or waveform processing analysis
60 (Arumugam et al., 2011) – through the identification of similar waveform char-
61 acteristics of repetitive signals. However, the complexity around accurate in-
62 terpretation of the AE activity by the user prevails in each considered method.

63 Hence, to support the process of interpretation of AE signals, it seems useful to
64 approach AE analysis through the scope of reverse engineering. Due to direct
65 visible access to the fingerprint of the source activity on the fracture surface,
66 cracking phenomena seem to present a suitable activity of interest for such in-
67 vestigation. The complete picture of the link between AE activities, state vari-
68 ables, fracture mechanisms and fingerprints on the post-mortem fracture sur-
69 face might provide valuable information for the design of robust and reliable
70 NDT algorithms.

71 To achieve a holistic understanding of source mechanisms during fracture
72 experiments of classical quasi-fragile material, this work proposes a multi-
73 modal experimental setup combining different NDT tools. With the purpose
74 of AE localization, crack tip detection and determination of crack front com-
75 plexities, combined time resolved AE, digital image correlation (DIC) and in-
76 volume measurements with post-mortem fracture surface analysis are applied
77 on cracking experiments, respectively. Each technique was considered to by-
78 pass the need of blind interpretation, while allowing to tie AE signals to frac-
79 ture surface patterns, i.e. enabling traceability of any captured AE signal to
80 the spatial position of the elastic waveform formation on the fracture surface.
81 Model experiments on PMMA are performed under predominant mode I load-
82 ing conditions leading to stable crack propagation, where heterogeneous crack
83 fronts generate high density of AE emissions with localized dynamic instabil-
84 ities, that are leading to high amplitude AE responses. Compared with proper
85 pure mode I experiments as a baseline and unstable alternate (stick-slip) crack-
86 ing (previously investigated in (Heinzmann et al., 2023)), the paper discusses
87 the complexity around the ability of correlating AE to local fracture regimes.
88 Such experiments may help the chain of understanding the connection of frac-
89 ture mechanisms and their AE signature.

90 The presented work is structured as following: at first, the experimental
91 setup is described by giving detailed information on the applied NDT methods
92 DIC, AE and crack front extraction. Thereupon, a metrological assessment of
93 AE source localization and DIC crack tip detection is presented to verify the
94 applicability of the established inverse problem and detection of the equiv-
95 alent elastic crack tip position w.r.t. complex crack fronts, respectively. The
96 presented work is then concluded by a discussion on the PMMA fracturing
97 through the multi-point view setup.

98 **2. Experimental program**

99 *2.1. Material, sample geometry and AE sensor placement*

100 Tapered double-cantilever beam (TDCB) shaped samples were obtained
101 from 8 mm thick molded PMMA plates (Plexiglas®) through laser cutting
102 (Class-4 laser system). To make intended in-volume recordings possible, only
103 transparent PMMA plates were considered. The sample geometry, as well as
104 AE sensor positions are shown in Figure 1. The coordinates ($x; y$) of the sensor
105 positions, with the notch tip as origin, are marked in red.

106 Two types of macroscopically stable crack propagation tests have been per-
107 formed:

- 108 a) Smooth quasi-static mode I crack propagation. Pin holes were drilled
109 manually to ensure perfect perpendicularity between pine hole axis and
110 sample face.
- 111 b) Same test as the first, however, the pin holes were machine drilled with
112 laser cutting. Here, clearance angles in the pin holes induces transverse
113 loads constraining the crack. The combination of normal axial loads with
114 supplementary transverse loads provoked cracking with a rough crack
115 profile and relatively intense AE activity.

116 With the objective of this work being the investigation of AE and crack growths
117 relationship, the second case has been considered to be a good candidate with
118 the pure mode I crack propagation case serving as reference. In the contin-
119 uation of the work, this type of cracking will be referred to as complex, while
120 referring to the reference case as smooth. The considered experiments with
121 their particular cracking type are summarized in Table 1. For discussion, the
122 presented data is combined with AE measurements from previous experiments
123 (?), where unstable crack propagation where analysed though the eye of linear
124 elastic fracture mechanics (LEFM) theory, without presenting the AE measure-
125 ments.

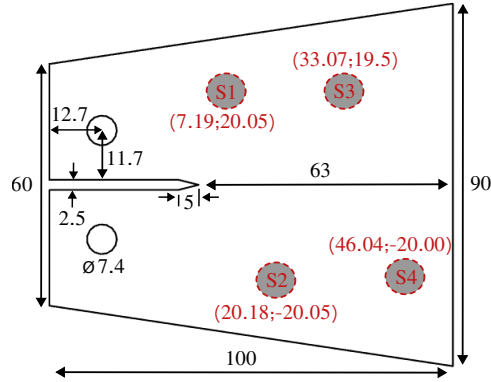


Figure 1: Sample geometry with the AE sensor positions and their coordinates (red) with respect to the notch tip [mm]. Radius of the notch tip is defined by the laser beam diameter of approximately $200 \mu\text{m}$.

Table 1: List of experiments.

Test	Cracking type
Reference	Purely mode I (smooth)
T5, T13	Predominantly mode I with bending (complex)

126 *2.2. Loading and test configuration*

127 Experiments were conducted with an ElectroPuls E10 000 Instron device
 128 with a load cell of 1 kN maximum loading capacity. The room temperature was
 129 controlled at 21°C. With a two staged loading procedure (?), influences of the
 130 notch tip on the cracking process were avoided. Extension rates of $0.01 \text{ mm}\cdot\text{s}^{-1}$
 131 were applied during the first loading stage initiating an approx. 1 cm pre-crack,
 132 while subsequent cracking was driven by extension rates of $0.07 \text{ mm}\cdot\text{s}^{-1}$.

133 *2.3. Experimental setup and methods*

134 The investigated crack propagation was simultaneously monitored by an
 135 AE system (MISTRAS Express-8) and a camera system with two high-resolution
 136 cameras (Viework VP-50MX-M/C 30). Each of the cameras, having different
 137 purposes, faced one side of the sample. One camera was used to perform DIC,
 138 while the other was used for in-volume fracture surface recordings of the prop-
 139 agating crack. This was achieved by placing the camera with an inclination to-
 140 wards the sample surface. Notice that in-place alignment has been checked to
 141 make face-to-face image registration straightforward. Lightning for the cam-
 142 eras was provided by multiple EFFI-Sharp PWR FF (Effilux) LED projectors.

143 The sample surface facing the camera intended for DIC measurements was
 144 coated with a speckle pattern. A form was designed and attached to the surface
 145 before coating the surface with regular spray paint, in order to ensure the best
 146 AE sensor to surface coupling by protecting the intended sensor positions from
 147 paint. Furthermore, consistent sensor placement from one test to the other
 148 was eventually achieved. Four AE sensors, positioned as visualized in Figure
 149 1, were used to capture AE activities. To improve AE localization, sensors were
 150 placed with horizontal offsets. Synchronous triggering of the systems was per-
 151 formed with a trigger box (R&D vision) being activated by the stage change of
 152 the Instron device. Like this, temporal accordance of the devices was achieved
 153 to simplify data comparison in the wake. A sketch of the experimental setup
 154 with a picture of a mounted sample is presented in Figure 2, while camera hard-
 155 ware parameters are given in Table 2.

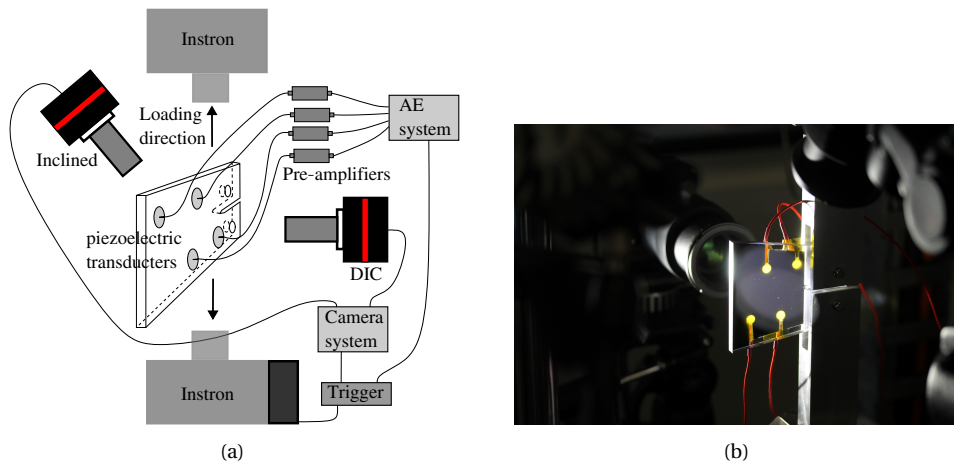


Figure 2: (a) Sketch of the experimental setup and (b) picture of an unbroken sample mounted in the mechanical device.

156 2.4. Digital image correlation (DIC)

157 By taking sequential images of the deforming sample, displacement fields
 158 can be obtained using DIC. It is based on the principle of conservation of
 159 brightness between reference (f) and deformed images (g) (equation of op-
 160 tical flow). This ill-posed non-linear inverse problem has the following form:

$$f(\underline{X}) = g(\underline{X} + \underline{u}(\underline{X})) \quad (1)$$

161 where $\underline{u}(\underline{X})$ presents the sought displacement field. The following ill-posed
 162 non-linear problem is eventually solved iteratively (Quasi-Newton method)

Table 2: Camera hardware parameters

Purpose	DIC	In-volume
Camera	Viework VP-50MX-M/C 30	
Image resolution	7856 × 1300 pix	
Acquisition rate	62.5 fps	
Lens	TOKINA 100 mm	
Aperture	f/2.8	
Field of view	37.18×6.15 mm	49.75×8.23 mm
Resolution	4.65 μm	6.17 μm
Patterning technique	Spray paint	

163 using FE-based quadrilateral elements and bi-linear shape functions. Further-
 164 more, with the displacement field obtained through DIC and a post-projection
 165 of the displacement field onto the Williams’ series expansion, fracture param-
 166 eter can be derived (Roux and Hild, 2006; Réthoré, 2015). Among others, the
 167 method allows for the detection of the crack tip position with a sub-pixel ac-
 168 curacy. For more details on the extraction of fracture mechanics parameters,
 169 the authors refer to the Appendix A presenting an extraction from (?). DIC
 170 and Williams’ series projection has been performed by using the library of the
 171 open-source software UFreckles (Réthoré, 2018), while required variables are
 172 listed in Table 3. Notice that in the context of this work only crack tip position
 173 will be analysed, with the projection zone (R_{min} and R_{max}) being defined by a
 174 parametric study. Furthermore, with DIC techniques working in pixels, a con-
 175 version variable is needed to find the corresponding metric/imperial data. Tak-
 176 ing an image of a ruler placed on the sample surface and using an FFT analysis,
 177 the pixel to meter conversion value is systematically obtained with a sub-pixel
 178 precision. Finally, a Savitzky-Golay filter (Polynomial), with a rolling windows
 179 of 50 ms, i.e. 3 frames, is applied on projected data.

Table 3: DIC & Williams' series parameters

DIC	
Software	UFreckles (Réthoré, 2018)
Discretization	FE-based global DIC
Shape function	Bi-linear quadrilateral Lagrange element (Q4P1)
Element size	95 μm
Post-filtering	Median filter using 1 st neighbour applied to U
Williams' series projection	
E	3.5 GPa
ν	0.32
R_{min}	127.8 μm
R_{max}	1301.6 μm
2D approximation	Plane-stress

180 *2.5. Acoustic emission(AE)*

181 AE analysis was performed with four resonant piezoelectric sensors
 182 (Medium Frequency resonant Miniature sensors Nano30 by MISTRAS). They
 183 have been mounted with conductive scotch and super glue. AE data was ob-
 184 tained by the AEwin streaming option to improve optimal recovery of AE ac-
 185 tivity by taking advantage of the short experiment duration (5 s). Hence, signal
 186 descriptors and waveforms were computed, through in-house Matlab scripts
 187 during post-processing. The AE responses were enhanced by a pre-amplifier
 188 with a gain of 40 dB, while background noise filtering through an imposed
 189 threshold was unnecessary since AE data was retrieved by streaming. The
 190 system was calibrated and tested for appropriate coupling before each test
 191 through the pencil lead break procedure (Scruby, 1987).

192 *2.6. Crack front identification*

193 Collecting information from within the volume, one would need CT scan
 194 techniques (Crandall et al., 2017) for the investigation of opaque materials.
 195 However, with PMMA existing as transparent material, capturing crack front
 196 kinematics is feasible with standard imagine techniques. To do so, the cam-
 197 era system has to be placed with an inclination to the sample surface causing
 198 experimental challenges in providing sufficient light and sharpness over the
 199 full sample length and thickness. Thus, lens and light settings were defined
 200 on a test sample, in which the crack propagated to about half of the sample

201 length. However, already tiny deviations from the crack path of this example
202 case led to strong local variations and losses in sharpness and light with respect
203 to each newly propagating crack. Hence, a compromised lens setting and light
204 positions had to be used to facilitate the recovery of the crack front kinemat-
205 ics for any possible crack path. For post-processing, a crack front extraction
206 algorithm was built along the following steps:

- 207 1. *Normalization*: To begin with, images were normalized to correct for
208 light variations between frames.
- 209 2. *ZOI*: A zone of interest (ZOI) around the crack front was defined, within
210 which the extraction was performed.
- 211 3. *Revealing advancement*: To reveal the advance of the crack front, preced-
212 ing images were subtracted from the current one. To increase robustness,
213 not only one preceding image, but the average of a pre-defined number
214 of preceding images was taken into consideration.
- 215 4. *Binarization*: A pixel threshold, based on the mean and standard devia-
216 tion (std) of the newly created image (step 3), was defined. This threshold
217 was used to binarize the image.
- 218 5. *Erosion and dilation*: The binary image was eroded (to remove unwanted
219 pixels) and dilated (to recover continuous objects).
- 220 6. *Boundary*: Tracing the boundaries of each object to define their pixel co-
221 ordinates by the MATLAB function `bwboundaries`, which is based on the
222 Moore-Neighbor tracing algorithm modified by Jacob's stopping criteria
223 (Gonzalez et al., 2004).
- 224 7. *Exclusion*: Excluding tiny objects with a minimum amount associated
225 pixels.
- 226 8. *Reconstruction*: Rebuilding the crack front mask based on the different
227 objects.
- 228 9. *Finishing*: Recovering a clean crack front by only considering the most
229 advanced position of the rough crack front mask.
- 230 10. *Smoothing*: Applying a moving median filter to reduce periodic trends
231 from outliers along the crack front.

232 It is worthwhile mentioning that the difficulties in recording sharp images of
 233 the in-volume crack propagation resulted in the algorithm partially not being
 234 able to clearly identify and extract the crack front. This is particular prominent
 235 along the edges of the crack front.

236 **3. Metrological assessment of crack tip detection and AE localization**

237 *3.1. Assessment of AE source localization*

238 *3.1.1. Methodology*

239 The method of AE source localization is a widespread addition to standard
 240 AE analysis. With the use of multiple AE transducers, depending of the in-
 241 tended dimension of observation, AE localization can provide information on
 242 the origin of an AE signal. While the accurate definition of wave velocity is key
 243 to the precision of traditional methods of AE source localization (e.g. (Schmidt,
 244 1972; Schau and Robinson, 1987; Abel and Smith, 1987; Romhany et al., 2017;
 245 Zhou et al., 2018)), recent studies focus on the development of wave velocity
 246 independent AE source localization methods (e.g. (Ciampa and Meo, 2010;
 247 Dehghan Niri and Salamone, 2012; Dong et al., 2019)). A review focusing on
 248 sensor quantity, investigated structural geometries and method performance
 249 of the different existing localization techniques is presented in Hassan et al.
 250 (Hassan et al., 2021).

251 For the presented work, an inverse problem for AE source localization –
 252 treating wave velocity as unknown – is proposed using four AE transducers.
 253 While this problem presents itself as ill-posed (Zhou et al., 2021), it can easily be
 254 build for multiple sensors (here, $n = 4$). Based on proportional relationships of
 255 distances and travel times between source and sensors, 2D source coordinates
 256 can be expressed by the nonlinear governing equation, with the assumed AE
 257 source location (x_s, y_s) and sensor positions (x_i, y_i) for all i from 1 to n . The
 258 equation is taking the following form:

$$(x_i - x_s)^2 + (y_i - y_s)^2 - v^2(t_i - t_s)^2 = 0, \quad \forall i \in [1, n] \quad (2)$$

259 where t_i and t_s are the arrival time of the signal at each sensor and the time
 260 the signal has been released at the source, respectively. To linearize such non-
 261 linear and coupled equation, variables x_s, y_s, t_s and v are substituted, respec-
 262 tively, by $x_o + dx, y_o + dy, t_o + dt$, and $v_o + dv$. These linearized contributions
 263 of Equation 2 then take the following form:

$$(x_i - x_s)^2 = (x_i - x_o)^2 + 2dx(x_i - x_o) + dx^2 \quad (3)$$

264

$$(y_i - y_s)^2 = (y_i - y_o)^2 + 2dy(y_i - y_o) + dy^2 \quad (4)$$

265

$$-v^2(t_i - t_s)^2 = -(v_o^2 + 2dv_o + dv^2)[(t_i - t_o)^2 + 2dt(t_i - t_o) + dt^2] \quad (5)$$

266 where x_o , y_o , t_o and v_o are the initial guesses with the current increments dx ,
267 dy , dt and dv .

268 After neglecting squared and weakly coupled terms, Equation 2 extended by
269 Equations 3, 4 and 5 leads to a four equation four unknown linear system.

$$L = 2 \begin{bmatrix} x_i - x_o & y_i - y_o & -v_o^2(t_i - t_o) & v_o(t_i - t_o)^2 \end{bmatrix} \quad (6)$$

$$b = [(x_i - x_o)^2 + (y_i - y_o)^2 - v_o^2(t_i - t_o)^2] \quad (7)$$

270 The system is eventually solved in a least squares minimization process as fol-
271 lowing:

$$L^T L = L^T b \quad (8)$$

272 3.1.2. Uncertainty

273 To evaluate the performance of the AE source detection and identify pos-
274 sible weak spots in the method, localization has been performed on synthetic
275 AE signals. To mimic the localization of AE signals, time of arrivals (TOA) of
276 the synthetic AE signals for all four sensors had to be computed. For this, the
277 following elements were considered:

- 278 • Young's modulus (E) = 3.5 GPa
- 279 • Material density (ρ) = 1200 kg.m⁻³
- 280 • Velocity (v) = $\sqrt{E/\rho}$ = 1707.8 m.s⁻¹
- 281 • Distance to the sensors i (d_i) = $\sqrt{(x_i - x_s)^2 + (y_i - y_s)^2}$, with (x_i, y_i) and
282 (x_s, y_s) being the sensor and source coordinates, respectively.
- 283 • Time of arrival (TOA_i) = d/v

284 In the following, (a) the influence of the initial guess position on the localiza-
285 tion uncertainty for various random source position and (b) the influence of
286 synthetic AE signals corrupted by expected experimental biases are investi-
287 gated.

288 Firstly, the non-linear problem is highly sensitive to the initial guess. To
289 highlight this sensitivity, localization error due to the initial guess has been
290 mapped for various random source positions. For each random position of AE
291 source, the AE localization was performed for a grid of 50x50 initial guesses. As
292 illustration, the initial guess error map is presented in Figure 3 for four random

293 AE source positions along the expected experimental crack path. σ denotes the
294 distance between the located source position and its real location. The figure
295 reveals that for some initial guess (yellow areas), the algorithm may not only
296 poorly converge but even diverge which highlights the strong initial guess de-
297 pendency. In practice, the cost function is not always convex depending on the
298 source location, so no convergence may be achieved leading to areas of 'for-
299 bidden' initial guesses. Furthermore, no particular initial guess area leading to
300 good localization ($\sigma \approx 1$ mm) for any potential source position was detected
301 within the field of interest. Hence, an evaluation to find the most suitable initial
302 guess has to be performed before each source localization run, i.e. any new
303 sought for AE signal requires its own optimal initial guess identification. This
304 can easily be achieved a priori knowing the crack tip position from DIC and
305 using the proposed numerical twin being presented in this section.

306 Secondly, to shift the model scenario closer to a real case, main order exper-
307 imental biases are introduced to the process of localization. A random normal
308 distributed error was drawn and appropriately scaled for each term of interest.
309 The target term with their standard deviation of the imposed uncertainty can
310 be found in Table 4. The potential errors for sensor placement, TOA and veloc-
311 ity were determined with respect to AE transducer radii of 3.7 mm, AE temporal
312 resolution of $0.1 \mu\text{s}$ and expected wave speeds of $1707.8 \text{ m}\cdot\text{s}^{-1}$, respectively. It
313 is worthwhile mentioning that the TOA has been identified as the most critical
314 variable for a successful AE source localization. A rather large uncertainty was
315 thus introduced here (about 10 times the AE sampling) to stress-test the algo-
316 rithm. Indeed, signals need on average $10 \mu\text{s}$ to propagate through the field of
317 view presenting, on average, a signal to noise ratio of 90% on the TOA. How-
318 ever, when the source goes closer to one of the sensors, since the uncertainty
319 is kept at $1 \mu\text{s}$, the signal to noise ratio decreases a lot with the propagation
320 time going closer to the uncertainty floor. Furthermore, identification of the
321 TOA through cross-correlating waveforms – to achieve sub-resolution accura-
322 cies – was not possible with waveform characteristics changing from one sen-
323 sor to the other (see Appendix C). While regular threshold crossing and float-
324 ing threshold crossing are the most basic methods of TOA detection, more ad-
325 vanced methods are proposed in literature. Cheng et al. (Cheng et al., 2021)
326 compared such methods in the case of I-shaped steel girder. With large dif-
327 ferences in peak amplitude, the TOA was determined in the presented work
328 through a dynamic threshold and verified by the Akaike Information Criterion
329 (AIC) method (Hensman et al., 2010). The dynamic threshold was defined as
330 twice the standard deviation of the absolute volt amplitude. It was additionally
331 possible to control and potentially adapt the TOA, due to the rather manage-
332 able amount of AE hits.

Table 4: Standard deviation (uncertainty) added to synthetic source position, time of arrival and first guess of velocity.

Error	Standard deviation
Sensor position	500 μm
TOA	1 μs
Velocity	5 $\text{m}\cdot\text{s}^{-1}$

333 Various AE source locations were tested to evaluate the performance of the
334 localization algorithm with respect to different areas of the field of interest.
335 Figure 4 is showing the uncertainty (in x and y direction) of the source local-
336 izations spanning a 20×20 grid. Each localization is presented as the median
337 absolute deviation (MAD) of the 200 iterations with changing copies of noise.
338 A priori identified optimal initial guesses however were kept constant for all
339 200 runs. Highest uncertainties (MAD around 20 mm) for the localization are
340 shown in yellow, while good identification of the source (MAD below 1 mm)
341 are shown in dark blue. With higher accuracies in the vicinity of the barycenter
342 of the four sensors, two main areas of weak performance can be observed be-
343 low sensor one and above sensor four. Hence, with the localization accuracy
344 showing strong local variations, uncertainties have to be evaluated independ-
345 ently for each localization attempt. However, with a red rectangle indicating
346 the area of observed experimental crack paths, the activities of interest do not
347 fall into the zones of highest uncertainties. Thus, high uncertainties should be
348 avoided.

349 Ultimately, the evaluation of uncertainties shows that localization of exper-
350 imental AE signals will need to consist out of the evaluation of the best suiting
351 initial guess and the area dependent localization uncertainty. The later will be
352 indicated by an error envelope (red dashed ellipse) around the detected source
353 position for any detected AE signal. In the context of this work, due to the infe-
354 rior spatial localization accuracy, AE localization does not compete against DIC
355 crack tip detection, but as support to verify the link between the propagating
356 crack and the AE activity. With no a priori existing proof that AE signals are ac-
357 tually emitted by the creeping crack, one needs to account for the risk of linking
358 potential noise signals to the crack. Moreover, it is worthwhile mentioning that,
359 considering through thickness variation of the crack front ($\pm 600\mu\text{m}$), the 2D
360 AE localization will not provide valuable information for discriminating from
361 which part of the front the AE has been emitted. However, sensibility of the
362 method to in-volume variations has still been evaluated (not presented here),
363 showing no particular additional bias on in-plane localization, other than on
364 the velocity identification.

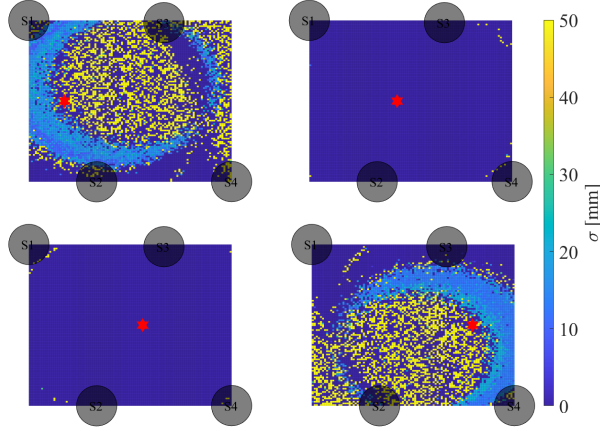


Figure 3: Map representing the sensitivity of the initial guess (50×50 grid) on the localization error for four AE source positions along the expect crack path. σ denotes the distance between the located source position and its real location (red star). Sensors are presented in scale of the real sensor base area with the area of interest being approx. 40×40 mm (see Figure 1)

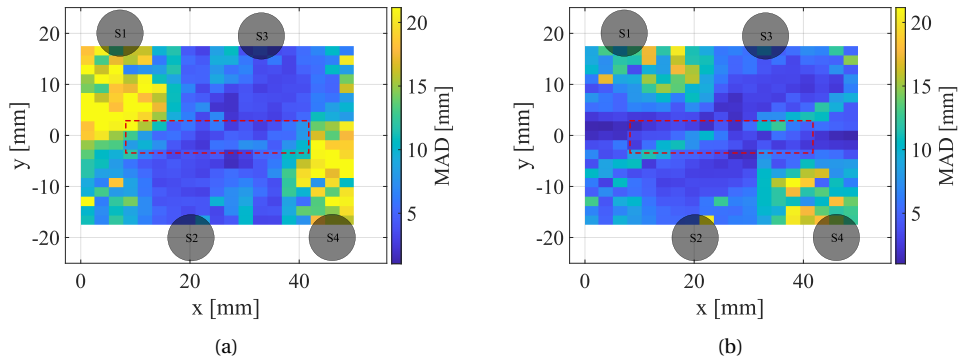


Figure 4: Median absolute deviation (MAD), i.e. mean identification uncertainty discarding outliers, on source localization depending on the source position (20×20 grid) for (a) x-direction and (b) y-direction. Sensors are presented in scale of the real sensor base area. The red rectangle indicates the area of observed experimental crack paths.

365 **3.2. Assessment of crack tip detection from DIC**

366 In literature, using DIC displacement fields and Williams' series expansion
 367 has become a classical method for the identification of the crack tip position
 368 (Hamam et al., 2007; Roux et al., 2009; Henninger et al., 2010; Réthoré and Es-
 369 tevez, 2013; Réthoré, 2015; Roux-Langlois et al., 2015). However, while a nu-

370 merical investigation with a curved crack front in (Réthoré et al., 2011) esti-
371 mated the apparent elastic crack tip position systematically in front of its free
372 surface appearance, it has not been explored experimentally. Here, we have
373 tried to elucidate this question through in-volume recordings of transparent
374 PMMA plates with the back-face inclined camera. Thanks to temporal syn-
375 chronization of the devices, each DIC frame had a corresponding in-depth
376 image visualizing the crack surface at this time. By taking the pixel to meter
377 conversion values of the two cameras into account, spatial matching was per-
378 formed by taking the notch tip as common reference point. Like this, as pre-
379 sented in Figure 5, detected crack tip positions were found in the in-depth vi-
380 sualizations of the fracture surface. Here, the crack tip detection on the DIC
381 side and within the in-volume images are presented for the first ((a) and (c))
382 and last ((b) and (d)) frame of experiment T13, respectively. The white rectan-
383 gle in Figure 5(a) and (b) is showing the field of view (FOV) of the DIC process.
384 In Figure 5(c) and (d), the DIC face is found on the upper side of the fracture
385 surface, with the red dashed line indicating the the crack tip position detected
386 by DIC through the thickness of the sample and the crack front highlighted in
387 green retrieved by the crack front extraction algorithm (see Section 2.6). By
388 taking the constant uncertainty on the determination of the notch position in
389 the images (approx. 20 pix) and on the pixel to meter conversion ratio from the
390 FFT analysis (approx. 1.27×10^{-4}) into account, the global uncertainty on the
391 DIC crack tip detection has been found to be not more than $45 \mu\text{m}$ (see (?) for
392 details). By taking all the above into consideration, the following points can be
393 observed:

- 394 • Evaluated uncertainties are lower than the in-depth crack front varia-
395 tions.
- 396 • Despite the in-depth crack front complexity, the crack tip is systemati-
397 cally detected at the position of the crack front on the DIC face.

398 Hence, DIC-based estimation of the crack tip position is suggested to be the
399 estimation of the crack tip at the surface and not an in-depth average. The
400 presented experiment, with a highly heterogeneous crack front made of mul-
401 tiple ligaments progressing and nucleating at different rates shown by bright
402 white lines in Figure 5(c) and (d), eventually shows that DIC-based crack tip
403 detection does not fully render such in-volume complexities.

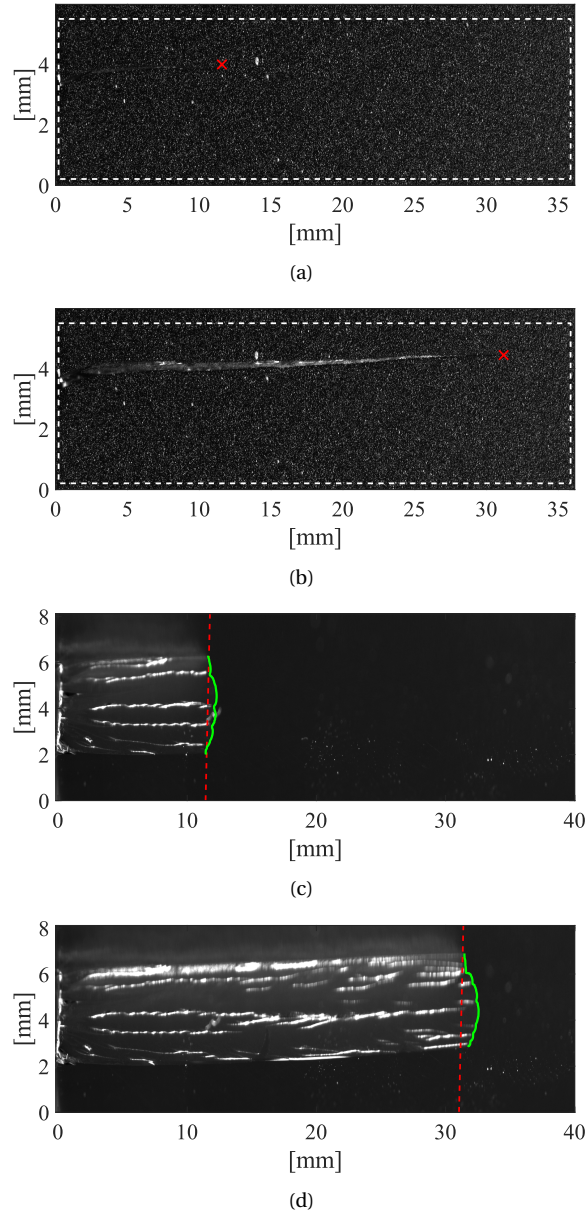


Figure 5: Accuracy in crack tip detection by Williams' series for first ((a) and (c)) and last ((b) and (d)) frame of the experiment T13. (a) and (b) shows the crack tip detection on the DIC face, with the white rectangle marking the FOV. (c) and (d) is showing the in-volume recording, where the DIC crack tip detection is vertically prolonged from the surface equivalent elastic crack tip position by the dashed red line and the crack front (obtained by the crack front extraction algorithm) is highlighted in green. The DIC face is found at the upper side of the crack surface in (c) and (d), while the maximal potential uncertainty in the equivalent crack tip detection related to the two frames is found to be approx. 40 and 45 μm , respectively.

404 **4. Results & discussion**

405 Fracturing of TDCB shaped PMMA samples were investigated through DIC,
 406 in-volume recordings, microscopy and AE. The time of interest for each exper-
 407 iment was 5 seconds during which, based on a common trigger (see Section 2),
 408 all time-dependent devices recorded simultaneously. Microscopic images of
 409 the fracture surface were obtained by a numeric microscope (Keyence) with a
 410 spatial resolution of $2.53 \mu\text{m}/\text{pix}$. With DIC being a surface measurement tool,
 411 images obtained by the inclined camera provide in-volume understandings of
 412 crack front complexities to account for deviations of the crack tip location mea-
 413 sured on the DIC face to the crack front within the volume. Eventually, AE lo-
 414 calization is performed to confirm that AE signals are actually emitted within
 415 the vicinity of the crack front and thereby avoid any misconceptions by po-
 416 tential environmental noise. DIC displacement fields and their corresponding
 417 Williams' series projections are presented in Figure 6.

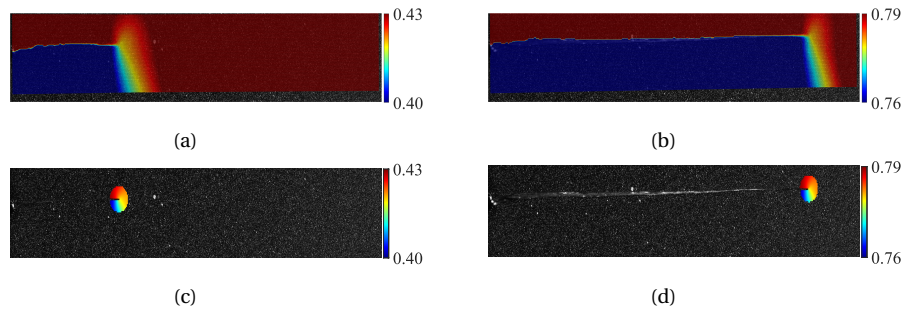


Figure 6: Vertical displacement field [mm] and corresponding Williams' series projection [mm] within the domain surrounding the crack-tip (defined by R_{min} and R_{max}) of the first and last recorded image for experiment T13. The used Williams' series parameters are listed in Table 3.

418 *4.1. Distinctive macroscopic features of the cracking cases*

419 As introduced earlier, two propagation scenarios – a reference (smooth
 420 model crack propagation) and two complex cracking experiments (closer to
 421 real case life cracking scenario) – have been investigated from surface kin-
 422 ematics and acoustic emissions points of view. More precisely, a pure mode I
 423 fracture experiment is denoted as reference, with T5 and T13 presenting com-
 424 plex fracturing experiments. Let us start from a macroscopic perspective. By
 425 presenting the three experiments in the space of normalized crack length as
 426 a function of experimental time (Figure 7(a)) and velocity as a function of the
 427 normalized crack length (Figure 7(b)), their difference in cracking behavior is
 428 highlighted. The normalization of the crack length is done with respect to the

429 maximal possible crack propagation distance of 63 mm, imposed by the sam-
 430 ple geometry (Figure 1). The crack propagation of the first loading stage, i.e.
 431 pre-crack, is leading to slightly (± 3 mm) different starting positions of the crack
 432 length for each experiment. Apart from really tiny steps in T5 (at 2.4 s, 3.2 s and
 433 4.2 s) and T13 (at 2.25 s and 3.0 s), crack propagation differences are almost un-
 434 recognizable in the three cracking cases by focusing on the crack length evolu-
 435 tion. However, by taking velocities into consideration, disturbed propagation
 436 of the complex cracking cases becomes more prominent. With an imposed ex-
 437 tension rate of $0.07 \text{ mm}\cdot\text{s}^{-1}$, mean velocities of $4.6 \text{ mm}\cdot\text{s}^{-1}$, $3.9 \text{ mm}\cdot\text{s}^{-1}$ and
 438 $4.2 \text{ mm}\cdot\text{s}^{-1}$ are measured for the reference, T5 and T13, respectively. While
 439 rather tiny velocity oscillations ($\pm 0.5 \text{ mm}\cdot\text{s}^{-1}$) are found in the reference ex-
 440 periment, strong variations – reaching peak crack speeds of $20\text{-}30 \text{ mm}\cdot\text{s}^{-1}$ –
 441 are detected during experiments T5 ($\pm 3.9 \text{ mm}\cdot\text{s}^{-1}$) and T13 ($\pm 3.2 \text{ mm}\cdot\text{s}^{-1}$). Dif-
 442 ferences in crack behavior become further evident by taking the AE streaming
 443 data into consideration. Figure 8 is showing the unprocessed AE streaming
 444 output for all three experiments. Only limited AE activity is detected during
 445 the reference case experiment, which suggests that elastic waves, potentially
 446 released during this cracking, are below the experimental sensitivity of the AE
 447 sensors. For the presented results, the average noise level is found to be 3.5 mV
 448 (31 dB) for all experiments. However, no clear link between the AE activity
 449 along the test and the velocity variations of the complex cracking is found at
 450 this stage.

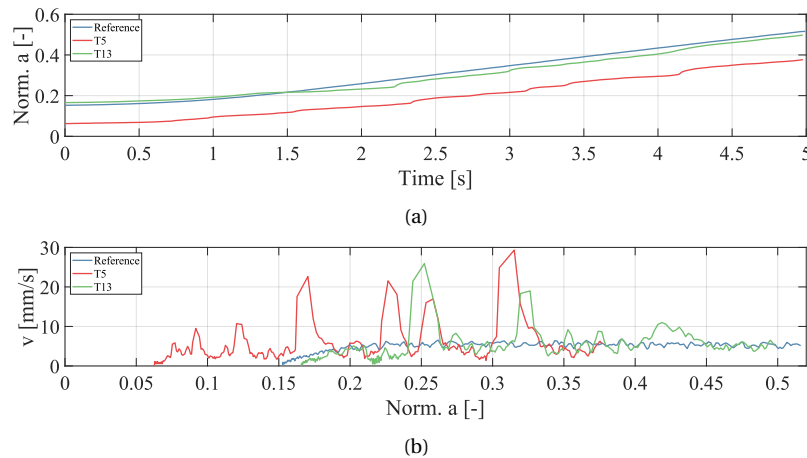


Figure 7: (a) Normalized crack length [mm] as a function of recorded time [s] and (b) velocity [mm/s] as a function of the normalized crack length [mm].

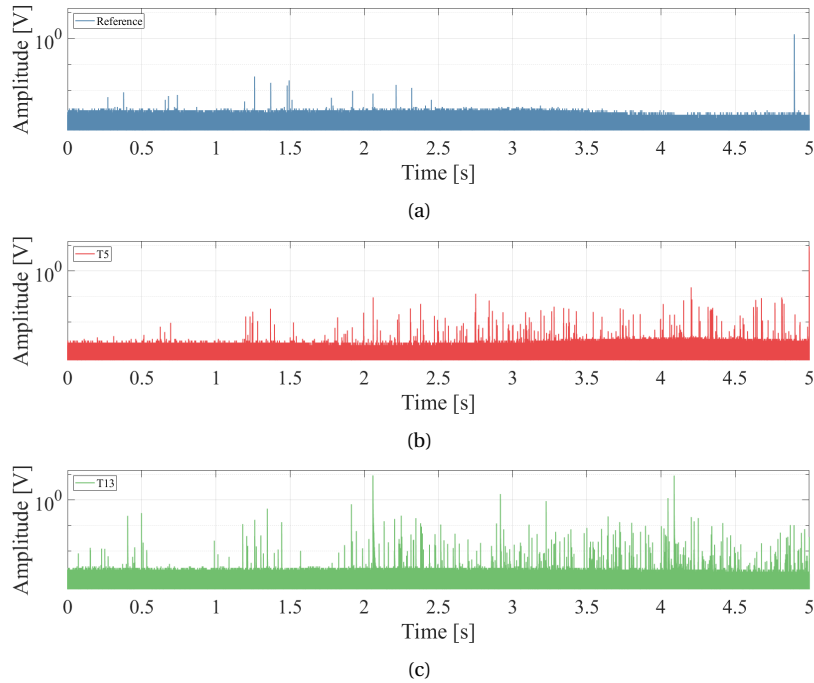


Figure 8: Raw AE streaming data (Amplitude [V] in log-scale vs. Streaming time [s]) of experiments (a) Reference, (b) T5 and (c) T13.

451 *4.2. Investigation of complex cracking cases*

452 Firstly, AE data will be investigated independently by cropping AE wave-
 453 forms from the streaming and the subsequent computation of AE parameters
 454 from those waveforms. By solely looking at the AE streaming output of experi-
 455 ments T5 and T13, strongly differing signals can already be identified within
 456 the set of AE responses. With peak amplitudes almost reaching 10 V (100 dB),
 457 these signals present a great variation to the average peak amplitude of ap-
 458 prox 0.01 V (40 dB) found for all other signals. To understand and identify their
 459 origin, we will focus on experiment T13, where two signals (at 2.1 s and 4.1 s)
 460 with a peak amplitude of 10 V are detected. To help analyse and classify the
 461 AE activity during this experiment, a Principle Component Analysis (PCA) – by
 462 taking all AE descriptors into consideration except Time and Threshold – has
 463 been performed on the entire set of recovered AE signals (see Appendix B for
 464 detailed information on the procedure). Underlining the discrepancy, Figure 9
 465 is showing both high amplitude (HA) signals in comparison with an example
 466 waveform of the lower amplitude (LA) signals, and the entire set of signals be-
 467 ing presented in the space of the most dominant principle component axis and

468 their AE descriptor contributions. While the differences in waveform charac-
 469 teristics are easily visible by comparing the two HA signals to the example of a
 470 LA signal, it is worthwhile mentioning that similarities comparing the two HA
 471 signals are found to be rather small. This becomes further evident by compar-
 472 ing all signals in the space of principle component axis. Indeed, three signals
 473 are found to be relatively far from the main cluster of signals that cover the
 474 space from approx. -5 to 5 along PC1 and PC2. Among these these signals, the
 475 two pre-defined high amplitude signal are the ones deviating the most from
 476 the rest presenting a local instability, where its origin is investigated in detail
 477 in the following section. However, with only a peak amplitude of 1 V, the third
 478 one (appearing at approx. 4.1 s shortly before the second HA signal) deviates
 479 from the majority of the lower amplitude signals, but does not compare to the
 480 HA signals being associated with local instabilities.

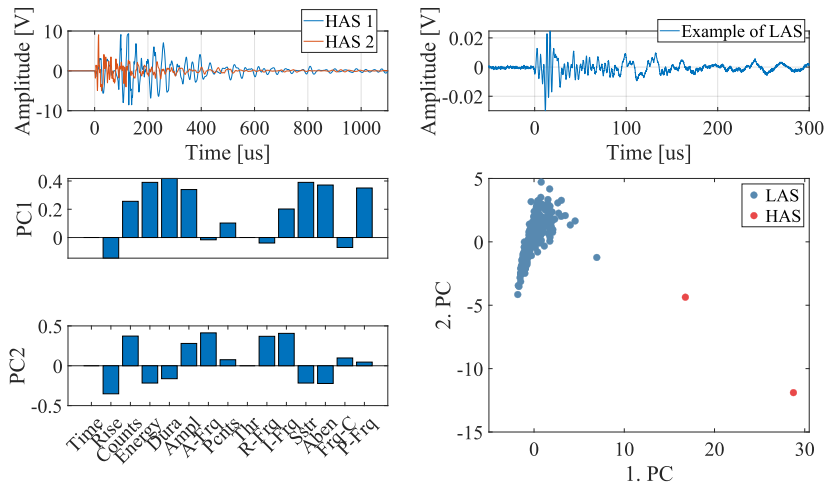


Figure 9: HA signals and an example of a LA signal, contributions to the two most dominant principle component axis (PC1 and PC2) and all AE signals presented in the space of first and second principle component.

481 4.2.1. High amplitude (HA) signals

482 To identify the origin of the HA signals, the position of their potential source
 483 activity needs to be spatially located on the fracture surface. As previously dis-
 484 cussed, the time of arrival of these signals can be associated to a frame of the
 485 DIC and inclined recording due to the device synchronization. Considering a
 486 camera temporal sampling of 16 ms and wave propagation times (from sensor to
 487 any potential source location) below 30 μ s, DIC and AE timelines can be
 488 matched without any shift correction. Hence, through means of DIC crack tip

489 detection and in-volume recordings, the position of the crack front at the po-
490 tential time of elastic wave formation can be identified. This conclusion only
491 holds true if AE signals are actually associated to the position of the DIC crack
492 tip. The crack tip is identified when any AE signal is received by the transducer
493 even in the case that the signal has not been released by the propagating crack.
494 To eliminate this question and avoid any potential misconceptions, AE source
495 localization was performed. Figure 10 shows the AE source localization of the
496 two HA signals. Black crosses indicate the current position of the crack front
497 (identified by DIC) at the time of the first AE threshold crossing. It is worthwhile
498 mentioning that the indicated crack tip position is the DIC crack tip detection
499 and therefore the position on the DIC face. Hence, no crack front complex-
500 ities – potential variations of $\pm 650 \mu\text{m}$ – are taken into account. Green dots
501 present the results of the AE source localization. As references, positions of the
502 AE sensors (S1, S2, S3 and S4) and the field of view (FOV) covered by the DIC
503 camera are presented with black circles and a dashed rectangle, respectively.
504 The dashed red ellipse indicates the identification uncertainty for this specific
505 source location based on our numerical twin (see Section 3.1.2). With both
506 signals being located within the zone of uncertainty, it is confirmed that the AE
507 signals have been emitted from or within close vicinity of the crack tip. Thus, a
508 deeper analysis of the fracture surface in the spatial vicinity of the crack front
509 for the two considered instants can be pursued.

510 Figure 11 is showing (a) the spatial evolution of the cumulative absolute
511 energy of the AE activity and the crack front at the instant of the two HA sig-
512 nals on the fracture surface, as well as (b) and (c) detail views of the fracture
513 surface. Crack propagation is from left to right with the notch tip at $x = 0 \text{ mm}$.
514 Smooth triangular zones, visible in fracture surface zooms (Figure 11 (b) and
515 (c)), are associated to unstable dynamic crack propagation. Macroscopically
516 smoother fracture surfaces are related to cracks propagating at speeds between
517 $36\text{-}200 \text{ m}\cdot\text{s}^{-1}$ (?). The recurrence of dynamic and quasi-static crack propaga-
518 tion with their fingerprint on the fracture surface have already been observed
519 in many studies (Ravi-Chandar and Balzano, 1988; Bonamy and Ravi-Chandar,
520 2003; Hattali et al., 2012; Vasudevan, 2018), and thoroughly investigated in
521 our recent work (?). Such dynamic instabilities, i.e. cracks suddenly jumping
522 over significant distances at average speeds of approx. $100 \text{ m}\cdot\text{s}^{-1}$, might be
523 induced by thermo-visco-elastic effects through rising temperatures at crack
524 tip (Vincent-Dospital et al., 2020). While large scale dynamic instabilities, un-
525 der purely mode I cracking conditions, can be provoked by particular exten-
526 sion rates due the existence of forbidden crack tip velocity domain for stable
527 crack propagation (see (?)), we observe that unsymmetrical through thickness
528 openings of the fracture front can lead to localized dynamic instabilities even

529 at slower extension rates (0.07 mm.s^{-1} instead of $>0.5 \text{ mm.s}^{-1}$ for large scale
530 instabilities). Indeed, the particular fracture surface markings, associated with
531 such cracking, are found in large scale and in the local scale.

532 As illustration, Figure 12 shows the raw streaming output with crack length
533 measurements of large scale instabilities during alternate cracking experiment
534 from our previous study (?). Here, dynamic crack propagation is defined by AE
535 signals with peak amplitudes of 10 V (100 dB) and vertical jumps in the tempo-
536 ral evolution of the normalized crack length. In comparison to these previous
537 experiments where the instability stretched smoothly along the entire sample
538 thickness, our current experiments present such mechanism localized on the
539 back side facing the inclined camera. To investigate if there is a potential con-
540 nection between energy released by the crack front in large scale and localized
541 dynamic instabilities, the relationship between AE absolute energy and surface
542 area spanned by the dynamic crack propagation has been analysed. In that
543 context, Figure 13 presents the AE absolute energy of dynamic bursts as a func-
544 tion of the burst area in semi-log scale. Signals of the dynamic bursts observed
545 during experiment T5 and T13 are being supplemented by those recorded dur-
546 ing alternate cracking experiments of our previous study (?). While cracks re-
547 leased AE absolute energies between 1.5×10^7 to 2.0×10^7 aJ to overcome areas of
548 approx. $10\text{-}130 \text{ mm}^2$ during alternate cracking experiments, AE absolute ener-
549 gies of approx. 6×10^6 , 5×10^6 and 2×10^6 aJ for areas of 0.34, 0.24 and 0.067 mm^2
550 were found for dynamic bursts during experiments T5 and T13. Figure 13 is
551 hence suggesting a linear relationship between the AE absolute energy and the
552 log of the crack propagation area. Results are presented for one sensor, while
553 no attenuation is expected due to travel small distances. However, it is worth-
554 while mentioning that the established relationship does not reflect the com-
555 plete fracture energy. Retrieved data solely relays on the punctual measure-
556 ment of the AE transducer. Thus, AE absolute energy measurements – com-
557 puted as the time integral of the squared voltage signal – bear a proportionate
558 and directional bias, while also relaying on the intrinsic transfer (potentially
559 complex) function of the sensor.

560 Furthermore, through the identification of local instabilities of the crack
561 front, crack velocity measurements can be reevaluated. For this, the crack front
562 was computed for each frame by the crack front extraction algorithm (Section
563 2.6). Before deriving the temporal evolution of the crack front to obtain the ve-
564 locities, the crack front displacements were smoothed over time by a second
565 order polynomial Savitzky-Golay filter over a window of three frames. Figure
566 14 presents, as a function of the recording time, the DIC determined crack tip
567 speed, the absolute voltage signal of the AE streaming and in-volume deter-
568 mined velocity map of the entire crack front. By comparing Figure 14 (a) and

569 (b), one can observe that the DIC crack speed increase (Figure 14 (a)) at 2.2 s ap-
570 pears, in time, approx. 100 ms after the detection of the local instability in the
571 AE streaming (Figure 14 (b)). This can be explained by the spatial position of
572 the dynamic burst along the depth of the sample. Taking Figure 14(c) into con-
573 sideration, local dynamic instabilities can be identified as crack front jumps on
574 the inclined camera face at around 16 mm and 27 mm. Hence, the first peak
575 in the DIC crack velocity can not be associated directly to the instability itself,
576 but rather to the crack front catching up belated with the strong local advance-
577 ment. It is worth mentioning, that the DIC-side velocities retrieved from the
578 crack front kinematics do match the apparent crack tip speed captured by DIC.
579 However, to enhance visualization of local velocity variations, the presented
580 velocity map in Figure 14(c) limited to an upper bound of 15 mm.s^{-1} . Thus,
581 velocity peaks around the local instabilities and their secondary impact on the
582 opposite side are saturated. As reference, the peak crack tip speed appearing as
583 secondary effect on the DIC face are found to be roughly 10 mm.s^{-1} lower than
584 directly measured through the in-volume recordings at the spatial position of
585 the instability. Nevertheless, velocities associated to the local instabilities have
586 to be taken with cautious, since sudden and strong velocity variations can not
587 be appropriately captured with the temporal resolution of the camera (16 ms
588 interframe). Hence, it has to be expected that the dynamically related velocity
589 variations are cropped in amplitude. In the vicinity of the second local instabil-
590 ity (4.1 seconds), Figure 14 (b) presents a more homogeneous increase in crack
591 front velocity along the sample thickness covering up potential secondary ef-
592 fects on the DIC face. However, while the first local instability (peak velocity of
593 about 34 mm.s^{-1}) was not strong enough to provoke a homogeneous increase
594 in crack tip speed along the entire sample thickness, no observable impact by
595 the second one (a peak velocity of about 22 mm.s^{-1}) can be expected on the
596 DIC face.

597 General observations of the crack front kinematics shown in Figure 14(b)
598 present a rather homogeneous crack front speed for about 2 s until the appear-
599 ance of the first local instability. Thus, it seems that this local instability pro-
600 duces a disturbance of the crack front behaviour resulting in global, periodic
601 accelerations and decelerations of the crack front with local velocity variations.

602 Finally, Figure 15(a) presents, as a function of the recording time, both crack
603 front velocity heterogeneity (computed as the standard deviation (σ) of the ve-
604 locity along the crack front at every time) and the AE streaming of experiment
605 T13. A clear correlation can be observed. Apart from some AE activity and tiny
606 velocity variations, the majority of AE activity and velocity variations are found
607 after the first dynamic instability at 2.1 seconds. Particularly around 2.1, 2.9,
608 3.5 and 4.1 seconds, good temporal agreement can be observed between the

609 increase in crack front velocity heterogeneity and the density of the AE activity.
 610 Underlining this correlation, Figure 15(b) and (c) present the interframe
 611 threshold crossings (counts), i.e. cummulative counts within a window of
 612 16 ms, as a function of the mean and standard deviation of the velocity along
 613 the crack front, respectively. The colorbar presents the experimental time.
 614 Both figures highlight the crack front disturbance introduced by the first dy-
 615 namic instability. Figure 15(b) clearly shows a separation of the homogeneous
 616 crack front phase with low AE activity (i.e. small number of interframe counts)
 617 from the heterogeneous crack front phase with high AE activity (i.e. high num-
 618 ber of interframe counts). However, the separation of these phases is not only
 619 found in time with the appearance of the local instability as disruption of the
 620 balance crack front propagation, but also by a crack front mean velocity (\bar{v})
 621 threshold of about 4 mm.s^{-1} . With the interframe count as a function of the
 622 crack front variations ($\sigma(v)$), Figure 15(c) is presenting a different angle on the
 623 correlation defined in Figure 15(a). A more heterogeneous crack front propa-
 624 gation results in a higher density of AE activity. Again, taking the experimental
 625 time into consideration, the first dynamic instability is found in the transition
 626 between the two phases.

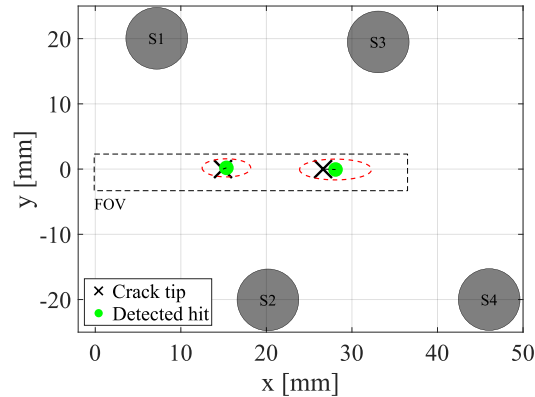
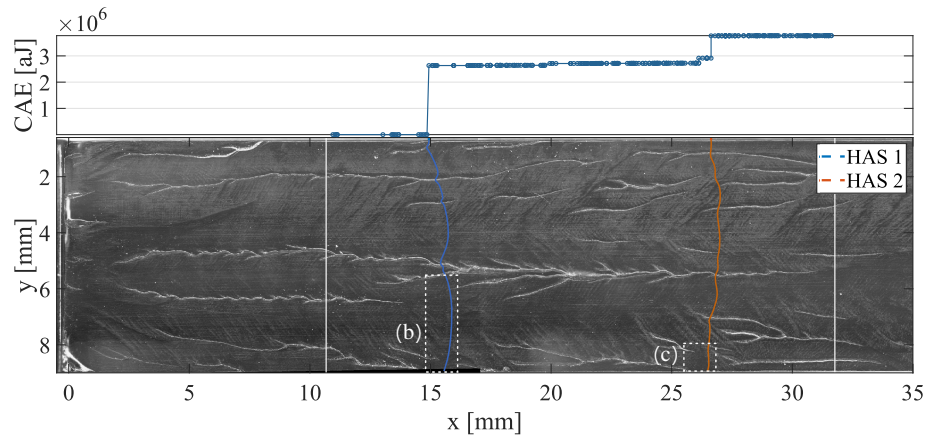
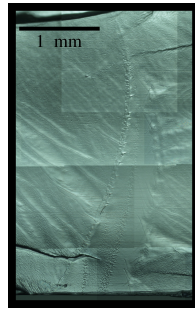


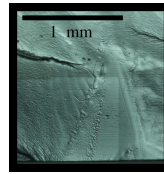
Figure 10: AE localization of the HA signals of experiment T13.



(a)



(b)



(c)

Figure 11: (a) Cumulative absolute energy (CAE) [aJ] of AE signals as a function of the crack tip position on the fracture surface with the crack front complexity for the two signals related to the dynamic bursts. (b) and (c) show a detailed view of the particular fracture surface markings associated to dynamic crack propagation.

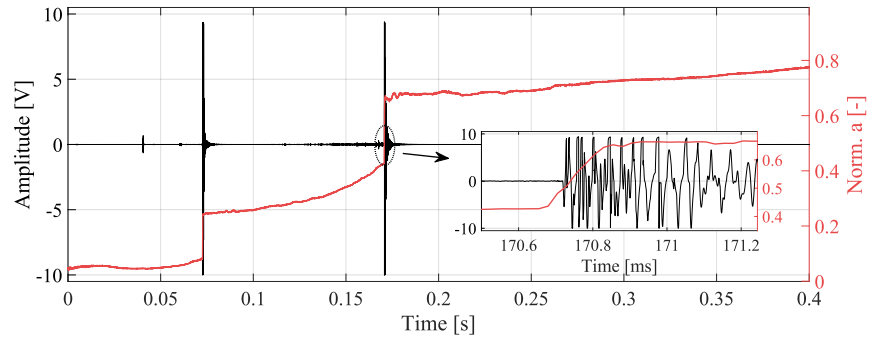


Figure 12: Normalized crack length [-] and amplitude [V] as a function of the recording time for an alternate cracking experiment.

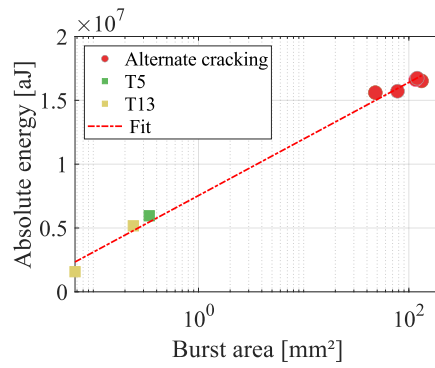


Figure 13: The AE absolute energy [aJ] as a function of the burst area (log-scale) for dynamic propagating cracks. Results are extended with data from alternate cracking experiments investigated in (?).

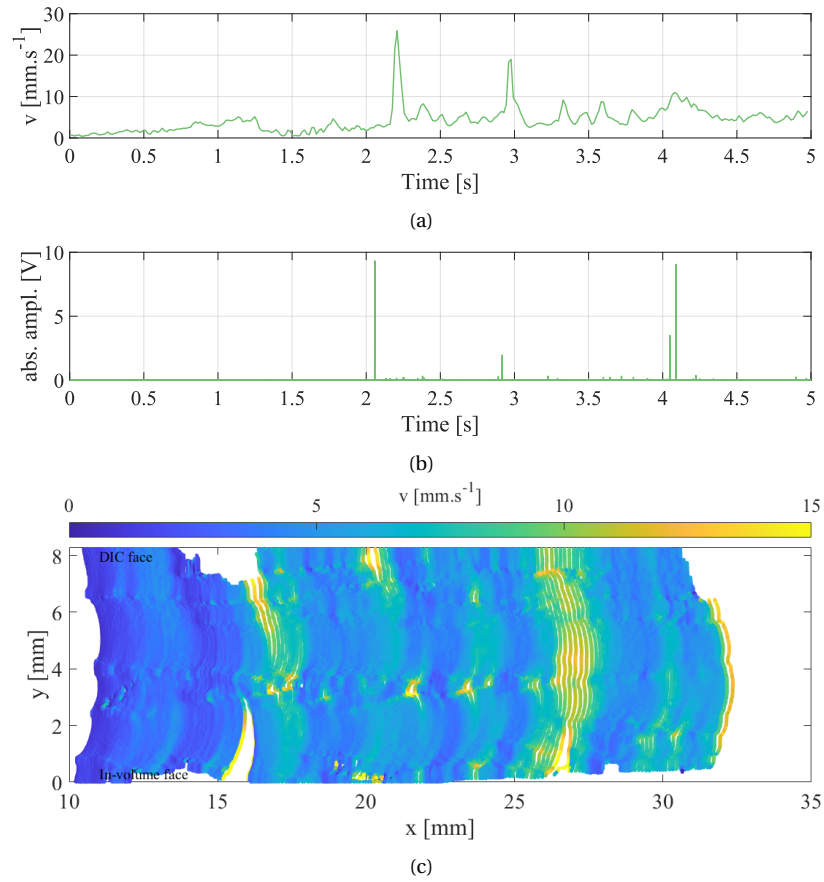


Figure 14: For experiment T13, (a) and (b) present, as a function of the recording time [s], DIC determined crack tip speed [mm.s^{-1}] and the absolute voltage signal of the AE streaming, respectively, while crack front velocities [mm.s^{-1}] along the sample thickness are shown in (c). Notice, white areas at the borders of the velocity map stem from the algorithm not being able to properly detect the edge of the crack front within the volume.

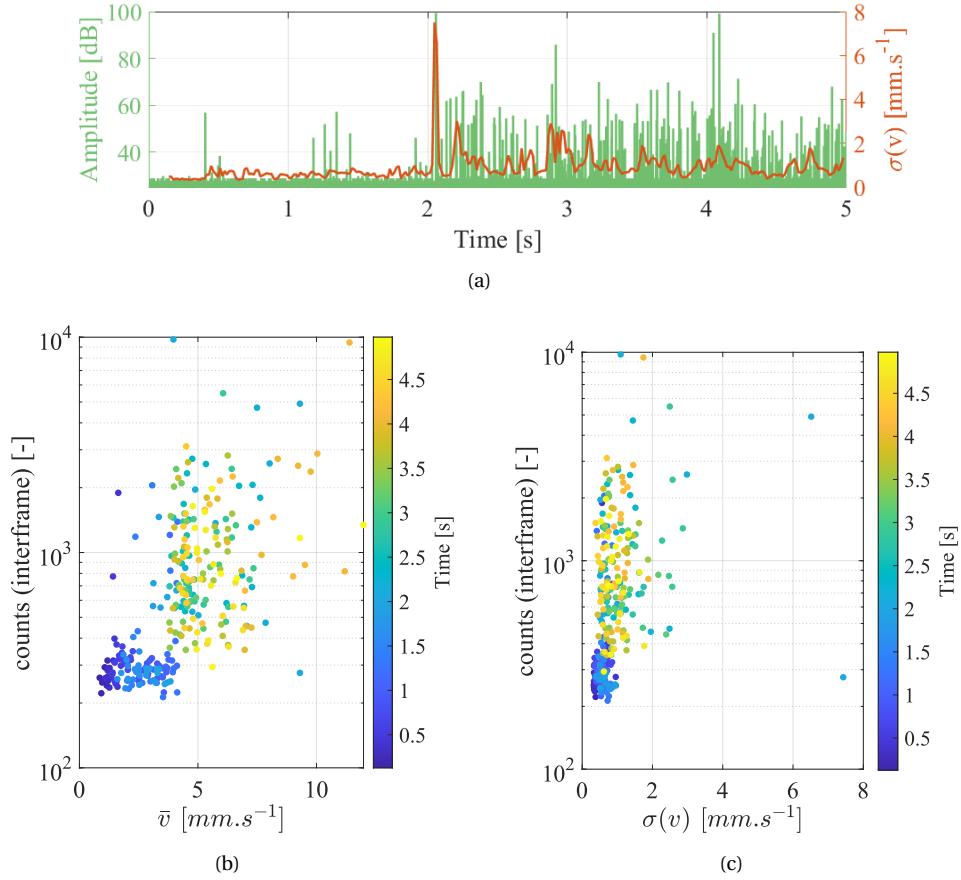


Figure 15: (a) AE streaming [dB] and the standard deviation (σ) of the velocity map [mm.s⁻¹] as a function of the recording time [s] for experiment T13. (b) and (c) present the interframe (16 ms) threshold (26 dB) crossings (counts) as a function of the mean (\bar{v}) and standard deviation ($\sigma(v)$) of the crack front velocity [mm.s⁻¹].

627 **4.2.2. Lower amplitude (LA) signals**

628 After discussing the origin of apparent crack tip speed variations, HA sig-
 629 nals evident relation to the localized dynamic instabilities, as well as clear con-
 630 nection between crack front velocity heterogeneity and the density/amplitude
 631 of AE signals, we will focus on the remaining lower amplitude (LA) signals. First
 632 of all, it is worthwhile mentioning that conclusions might differ with respect to
 633 the AE sensor used for performing the analysis. Even when the theoretical ap-
 634 plication of the AE method seems rather trivial, waves propagating at different
 635 velocities, while being reflected, dispersed and refracted, increases the diffi-
 636 culty of adequate interpretation of the recorded AE activity. Particularly in the

637 case of LA signals, the impact of each individual sensor, directionality of elastic
638 waves due to crack front complexities or the attenuation of signals from differ-
639 ent wave traveling distances result in the variation of waveform characteristics
640 of the same AE signal for different sensors. This has similarly been pointed out
641 by (Maillet et al., 2015) for the classification of damage modes in composite
642 materials. To underline this, a LA example signal is presented in the Appendix
643 C (Figure C.26) with their computed AE parameters (Table C.6) for all four sen-
644 sors. With extensive literature existing on the investigation and classification of
645 AE activity, the objective here is not to provide an exhaustive analysis of LA sig-
646 nals but underline, complementary to the previous part, intrinsic difficulties in
647 properly associating AE responses to source mechanisms and their fingerprint
648 on the fracture surface. Contrary to HA signals, where a straightforward link
649 between apparent crack velocity variations, AE responses and fracture surface
650 features can be established, LA signals are more numerous (somehow simi-
651 larly spread along the entire recording), while potentially being associated to
652 various and subtle fracture surface features. This section proposes to use the
653 developed experiment and analysis tools to discuss this complex relationship.

654 Firstly, the fracture surface of the reference and complex cracking case will
655 be compared by taking their AE activity into consideration. For this, a mi-
656 croscopic image of the post-mortem fracture surface of the two fracture cases
657 are presented in Figure 16. On the one hand, with almost no AE activity (see
658 Figure 8(a)), purely mode I cracking experiments in PMMA produce a surface
659 with symmetric, wave like ligaments (see also (Hattali et al., 2012; Vasudevan,
660 2018)). These waves are found almost parallel to the crack propagation direc-
661 tion with a tendency to the boundaries, while showing topographical varia-
662 tions of approx. $\pm 70 \mu\text{m}$. In addition, tiny regularly spaced waves (every ~ 50 -
663 $100 \mu\text{m}$), perpendicular to the crack propagation, are observed. These waves
664 may potentially be associated to small crack advances. On the other hand,
665 deep and unstructured scratches on a rather flat fracture surface are observed
666 during complex cracking cases, where strong AE activity is detected (see Figure
667 8(b) and (c)). At this stage, it seems reasonable to say that the change in AE ac-
668 tivity is mainly due to the discrepancy observed at macro-scale, i.e. scratching
669 marks.

670 For the classification of AE signals and their characteristics, plenty of an-
671 alytical methods are proposed in literature (e.g. waveform cross-correlation
672 (Deschanel et al., 2017), parametric clustering (Guo et al., 2017, 2022), wavelet
673 analysis (Sung et al., 2000), b-value analysis (Sagar et al., 2012), moment ten-
674 sor inversion (Grosse and Ohtsu, 2008)). For this study, the more specific
675 method of multiplet identification through waveform cross-correlation (De-
676 schanel et al., 2017) will be pursued. As the foundation of AE analysis, the

677 method relies on the assumption that similar waveforms are most likely related
678 to the same source mechanism. The identification of multiplets directly com-
679 pares signal characteristics by cross-correlating normalized waveforms to de-
680 fine highly correlated groups of signals, i.e. multiplets (nearly identical wave-
681 forms as signature of a unique source (Deschanel et al., 2017)). In the following,
682 LA signals will be investigated by waveform cross-correlation with the aim of
683 identifying AE signals, as in the case of HA signals, being linked to particular
684 fracture surface markings. To present multiplets in the AE descriptor Princi-
685 pal Component (PC) space, signals were firstly normalized in this case. Indeed
686 since multiplets are based on normalized waveforms, while e.g. amplitudes
687 and energies may vary from one signal to another within a particular multi-
688 plet, direct comparison between AE feature and multiplet classification would
689 be meaningless without an identical normalization in both techniques.

690 The identification of multiplets was performed only over the impulsive
691 part, i.e. the duration of a signal free of rebounding waves. Thus, only primary
692 waves will lead to the multiplet classification of signals. In the present case, the
693 impulsive part was defined to be $40 \mu s$ starting from a $5 \mu s$ pre-trig preceding
694 the detected time of arrival (TOA) of each waveform. A correlation coefficient
695 above 0.75 was defined for the collection of AE multiplets.

696 Figure 17(a) is showing the signals associated to two multiplets in the space
697 of the first and second principle component axis of the normalized AE param-
698 eters, with the contributions to the two principle components shown in Figure
699 17(b) and Figure 17(c), respectively. In the present case, due to normalization,
700 some meaningless features have been removed from the analysis: Time and
701 Threshold (as in the previous analysis of HA signals in Section 4.2.1), as well as
702 Energy, Signal Strength and R-frequency (see Appendix B for feature details).
703 When looking at Figure 17(a), clear multiplet separation is mainly observed
704 along the first principal axis. Hence, taking Figure 17(b) into consideration,
705 differentiation between AE signals associated to the two multiplets is driven by
706 rise time, count and duration. However, it is worth mentioning that a classifi-
707 cation, similar to multiplet, could not be achieved using neither k-means nor
708 DBSCAN unsupervised classification methods. Different explanation could be
709 proposed for such observation: (1) Multiplets are obtained from the impulsive
710 part ($40 \mu s$), while the AE descriptor are computed using the entire waveform.
711 Hence, the coda of the waveform makes the standard AE descriptor classifi-
712 cation less straightforward. (2) Figure 17(a) shows that the entire set of lower
713 amplitude signals are closely packed within the AE descriptor principal com-
714 ponent space. Thus, no clear separation can be observed in between multiplets
715 indicating that all signals share common features.

716 Furthermore, by identifying rise time, counts and duration as influential

717 waveform descriptors, one can define the RA-value (i.e. rise rime over ampli-
718 tude) and relate it to the average frequency (counts over duration). Figure 18
719 is presenting all AE hits and the multiplets in the space of these two variables.
720 For granular materials, the separation of AE hits in the space of average fre-
721 quency and RA-value has been correlated to tensile and shear fracture modes
722 (Aggelis, 2011; Noorsuhada et al., 2017). However, with limited information on
723 the source activity in the case of PMMA, Figure 18 allows solely for highlighting
724 the presence of two categories of AE signals, where the two multiplets are only
725 represented in one.

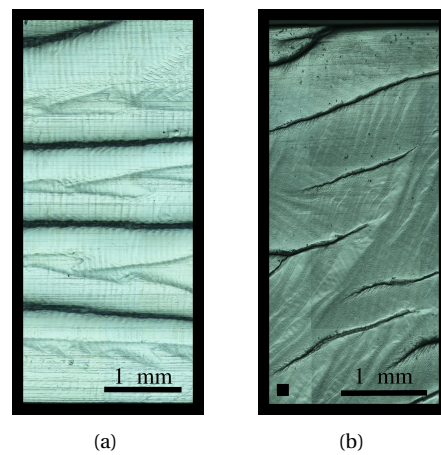


Figure 16: Microscopic image of fracture surface for (a) reference and (b) complex (T5) cracking case. Crack propagation is from left to right.

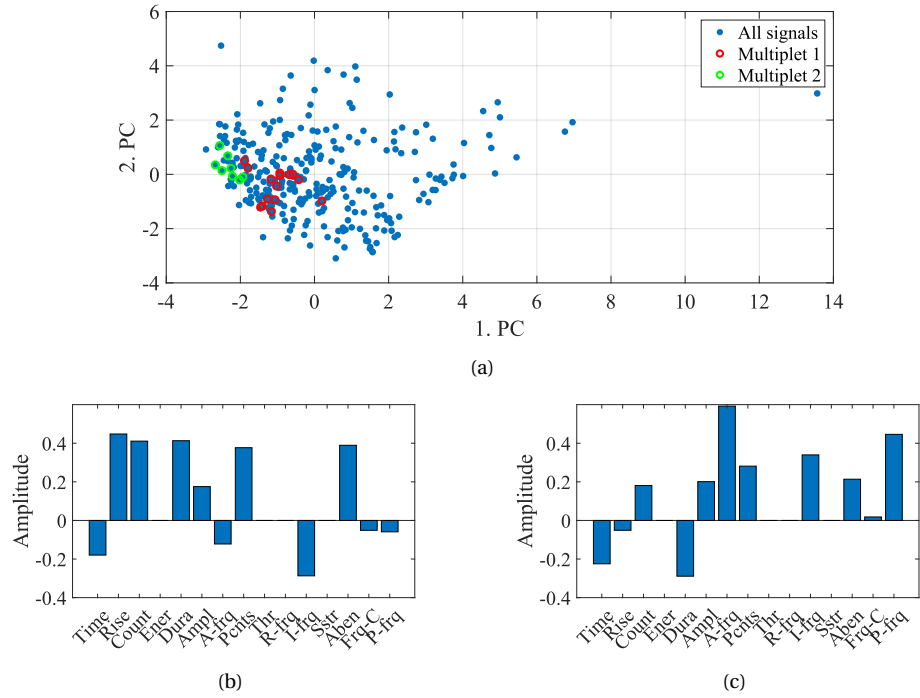


Figure 17: (a) Multiplet are presented in the space of first and second principle component axis of parameters computed from normalized AE signals, while (b) and (c) show the parametric contributions to the first and second principle component axis, respectively.

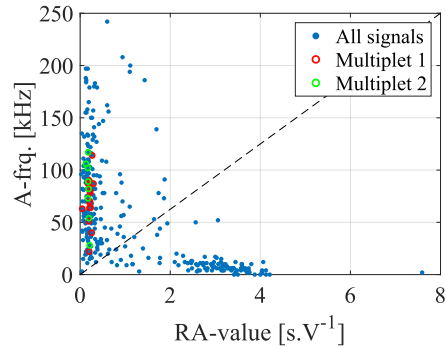


Figure 18: Average frequency [kHz] as a function of the RA-value (Rise Time over Amplitude) [s.V⁻¹].

726 4.2.3. *Multiplets vs fracture surface fingerprints*

727 The normalized waveforms of the two multiplets are presented next to the
728 histogram of their correlation coefficients in Figure 19, while AE localization
729 results are presented in Figure 20 to confirm the link between AE signals and
730 crack tip activity. Indeed, waveforms associated to the two multiplets show
731 to be highly similar over the duration of the defined impulsive part (40 μ s).
732 With an average correlation coefficient of 0.48 among all captured AE signals,
733 average (and lowest) correlation coefficient of 0.88 (and 0.77) and 0.92 (and
734 0.83) were found among AE waveforms associated to Multiplet 1 and 2, respec-
735 tively. Furthermore, information on the non-normalized waveforms presented
736 in Figure 19 are presented in Table 5. The position of the multiplets on the frac-
737 ture surface are shown in Figure 21. Notice that three signals (3-5) of Multiplet
738 1 appear within the same time frame and are thus linked to the same crack
739 front. Hence, while 15 waveforms are collected in Multiplet 1, only 13 crack
740 front lines are shown in Figure 21. Considering the high level of correlation
741 between signals of a multiplet, one would expect to observe fingerprints of a
742 similar source mechanisms during the fracture surface investigation. However,
743 after inspecting the fracture surface in the vicinity of the expected source activ-
744 ity, no particular reoccurring surface mark is observed. For both multiplets, no
745 repeating event can be unambiguously identified that is solely linked to their
746 expected position of waveform formation. In an attempt to understand such
747 observation, i.e. no clear macroscopic systematic fingerprint is observed at
748 each crack front position associated to multiplet emissions, an extrapolation
749 of Figure 12(b) is proposed. Indeed, following the observed linear relationship
750 between AE absolute energies and the log of the growth fractured area in the
751 case of dynamic instabilities (HA signals either macro or localized) and assum-
752 ing similar mechanisms but at much smaller scale, an expected crack surface
753 growth associated to multiplet signals can be estimated. With a difference in
754 the dimension of millions between the AE absolute energy of LA signals (below
755 235 aJ, see Table 5) and HA signals (above 2×10^6 aJ), propagation areas below
756 $\sim 22.7 \times 10^3 \mu\text{m}^2$ will be associated to LA signals. In the case of a homogeneously
757 propagating crack front, this would result in crack advances of approx. 2.8 μm
758 over the sample thickness of 8 mm for the strongest LA signal. If expressed as
759 a square with $\sim 151 \mu\text{m}$ sides, the sought for area is presented in Figure 16(b)
760 in the left bottom corner as reference. This underlines the difficulty to unam-
761 biguously identify systematic similar fracture surface fingerprints for LA sig-
762 nals with the naked eye. However, while more advance image analysis tools
763 may help, no obvious solution has been found in this work.

764 Nevertheless, Figure 15 has shown that link between AE and crack front

765 may be more connected to the actual kinematic of the crack front than on its
766 post-mortem characteristics. To take advantage of the observations in Figure
767 15 for the correlation of AE activity with crack front velocity heterogeneity, Fig-
768 ure 22 is proposing an identification of potential locations of the AE signal ori-
769 gin on the fracture surface based on crack front velocity heterogeneity. For this,
770 22(a) shows, as reference, a fracture surface extraction of the crack propagation
771 area during which the synchronized devices were active and 22(b) the velocity
772 heterogeneity of the crack front for each frame of the inclined camera record-
773 ing. The figure is supplemented with the AE hits positioned for HA signals at
774 both, (1) the right time (i.e. within the crack front associated to this particular
775 time) and (2) the velocity peak along the crack front and for LA signals just at (1)
776 the right time (i.e. within the crack front associated to this particular time). No-
777 tice, while positioning HA signals onto the peak velocity along the crack front
778 results in perfect identification of the source activity within the volume, one
779 can not assume the same for LA signals, since the multiplet signal does not
780 necessarily present the highest recorded AE signals associated to this frame.

781 Nevertheless, let us first focus only on the relation between the fracture sur-
782 face and the crack front kinematics. Interestingly, no particular difference in
783 terms of crack surface features can be identified with respect to the two phases
784 of homogeneous (10-15 mm) and heterogeneous (15-32 mm) crack front prop-
785 agation. However, velocity heterogeneity's – although different in scale – can
786 be seen in both phases in the vicinity of the artifacts (white marks) on the frac-
787 ture surface. Especially notable are the two local crack front jumps between
788 two consecutive frames at approx. 15.5 mm and 27 mm that are associated
789 to the first and second local dynamic instability, respectively. Extending the
790 discussion by the AE waveforms, the two dynamic instabilities – being already
791 well understood and localized during the previous discussion – are well iden-
792 tified (asterisk markers colored in magenta in Figure 22(b)) at the spatial posi-
793 tion of the dynamic instability along the thickness of the sample. Noteworthy,
794 the location of the dynamic instabilities has only been identified on the DIC
795 face up to this point. Its correct fracture surface location was detected through
796 pre-existing knowledge on fracture surface patterns associated to dynamic in-
797 stabilities. However, by taking the above into consideration, before made as-
798 sumptions have been evidenced.

799 With respect to AE signals being related to the multiplets, one can observe
800 that all signals appear during the more 'responsive' section of the streaming
801 (Figure 15) after the first dynamic instability. While the crucial information
802 provided by the through thickness crack front growth rate heterogeneity seems
803 to correlate the signals to local perturbations (scratches/artifacts) observed on
804 the surface, it did not provide an unambiguous explanation for the natural

805 multiplet classification.

806 This section, while presenting a side discussion, is a perfect example of
807 potential miss interpretation when dealing with partial AE data. Indeed, it is
808 shown that a large amount of highly similar signals – coming from the crack
809 tip – can not be systematically attributed, at least from post-mortem fracture
810 surface features, to a particular mechanism or behavior. While discriminat-
811 ing fracture phenomena on signal levels has been found to be straightforward,
812 classifying within signals of similar amplitudes have been found potentially
813 misleading.

Table 5: Information on non-normalized waveforms associated to the multiplets.

Multiplet	Peak amplitude range	Absolute Energy range (mean)
1	8.9 mV (39 dB) to 50 mV (54 dB)	7 aJ to 235 aJ (63 aJ)
2	7.9 mV (38 dB) to 25 mV (48 dB)	4 aJ to 50 aJ (28 aJ)

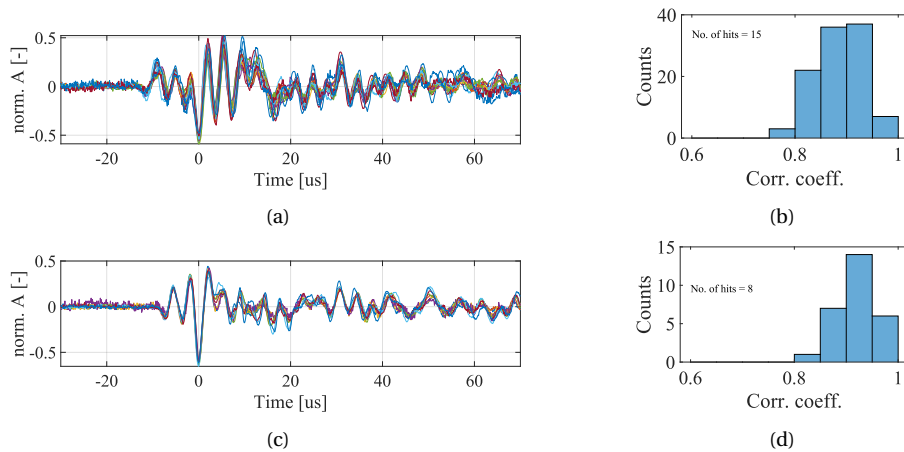


Figure 19: Normalized waveforms associated to (a) multiplet 1 and (c) multiplet 2, with their corresponding histogram of correlation coefficients ((b) and (d)).

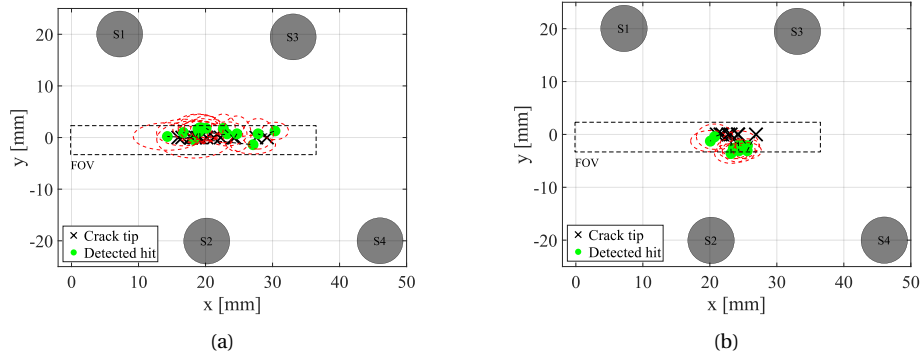


Figure 20: AE localization of (a) Multiplet 1 and (b) Multiplets 2.

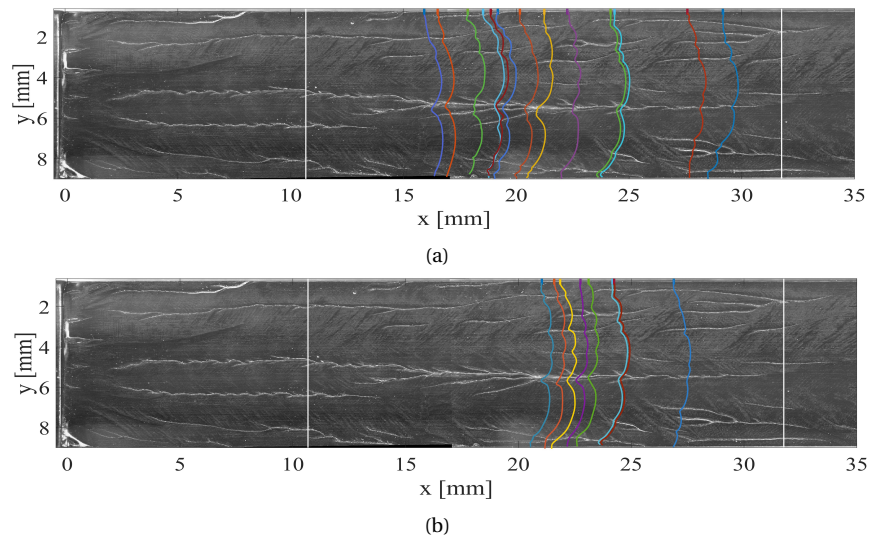


Figure 21: Crack front complexities related to waveforms associated with (a) Multiplet 1 and (b) Multiplet 2.

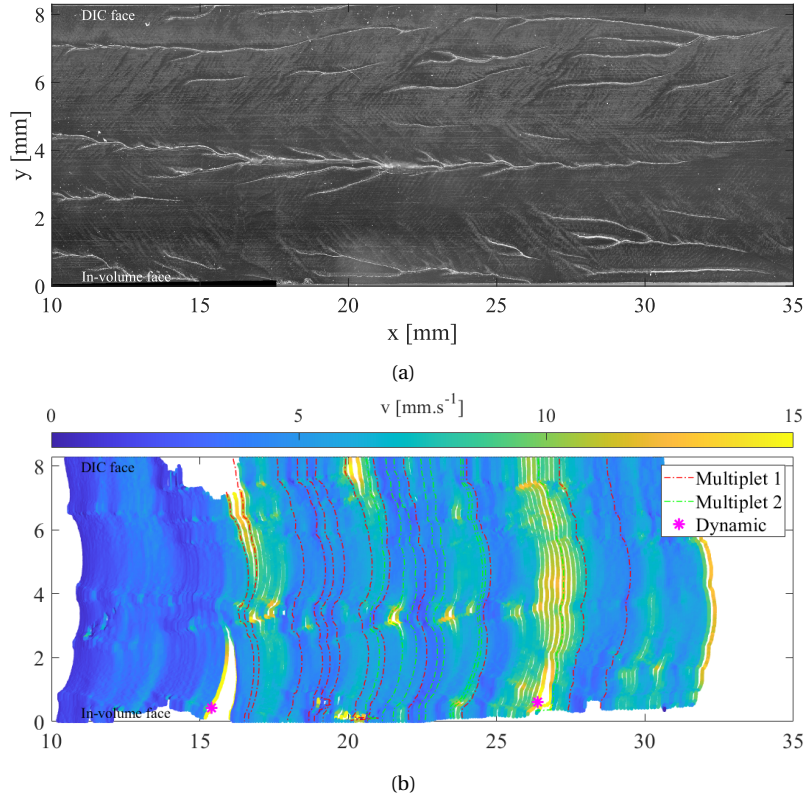


Figure 22: (a) Fracture surface crop over which the crack propagated during the experimental time and (b) corresponding crack front velocities [$\text{mm}\cdot\text{s}^{-1}$] presented on the extracted crack fronts from the inclined images.

814 5. Conclusion and perspectives

815 A model lab experiment under mode I dominating opening mode – with
 816 slight front/back opening asymmetry leading to complex cracking behavior
 817 and high AE activity – has been designed and studied through a multiple point
 818 view perspective. With the aim of linking source mechanisms of AE signals
 819 to post-mortem fracture surface characteristics, the combination of devices
 820 allowed for a holistic investigation of the fracturing process. DIC, in-volume
 821 recordings and the combination of multiple AE sensor was used for crack tip
 822 detection, identification of crack front complexities/kinematics and AE source
 823 localization, respectively. The analysis relies on both, automatic crack tip de-
 824 tection using DIC and Williams series expansion, as well as AE source localiza-
 825 tion.

826 The present work provides (1) a methodological/numerical and (2) physi-
827 cal contribution that are summarized in the following:

828 1. On the methodological side, it has been shown that:
829

- 830 • The ill-posed problem of AE localization, without a priori knowl-
831 edge on the wave speed, using multiple AE sensor is highly sensitive
832 to the initial guess when solving it with classical Newton-Raphson
833 algorithms. This issue can be partly overcome by designing an op-
834 timization procedure for the initial guess. It has been done finding
835 for each crack tip position the best initial guess parameters for con-
836 vergence using a simple numerical twin. Eventually, for the sensor
837 position considered in this work (not optimized), a localization un-
838 certainty lower than 2 mm can be achieved for most of the crack
839 propagation.
- 840 • An image analysis procedure has been proposed to capture the po-
841 sition and the kinematics of complex crack front using in-volume
842 recording in the case of a transparent material. It allows for cap-
843 turing local variation of the crack front kinematics, which has been
844 found highly valuable for connecting macroscopic AE activity and
845 crack front behavior.
- 846 • The combination of in-volume observations and apparent crack tip
847 position from LEFM theory and DIC, it has been shown that the ap-
848 parent crack tip position is closely related to the surface crack front
849 position and does not reflect crack front complexity by a through
850 thickness homogenization process. This point remained unclear in
851 the literature associated to crack tip detection using William's series
852 expansion and DIC.

853 2. On the physical interpretation side, the following points have been ob-
854 served:

- 855 • A systematic connection between AE activity and crack front posi-
856 tion has been demonstrated using both apparent crack tip detec-
857 tion, through DIC/Williams' series expansion, and AE localization.
- 858 • Combining AE streaming and in-volume crack front kinematics
859 data, a strong correlation between amount and intensity of acoustic
860 emission and heterogeneity of the crack front kinematics has been
861 observed. Indeed, while homogeneous crack front velocity does not

862 produce signals, at least high enough to leave noise floor, once the
863 crack front kinematics become heterogeneous, strong AE activity
864 occurred. It explains the difference in term of AE activity observed
865 between pure mode I and perturbed mode I experiments in PMMA.
866 This observation is highly valuable since it demonstrates that post-
867 mortem analysis could be misleading in term of AE source mech-
868 anism analysis, since it does not necessarily reflects the transient
869 kinematics of the front.

- 870 • Different families of AE signals have been observed: High ampli-
871 tude (HA), a dominant class of lower amplitude (LA) signals and
872 among them two multiplets, i.e. set of signals having highly cor-
873 related impulsive waveform parts.
- 874 • A connection between dynamic instabilities of intermittent stick-
875 slip phenomenon produced macroscopically in PMMA when crack
876 growth rates reach the forbidden velocity domain (see (?)) and of
877 the front/back asymmetric experiments during dominant mode I
878 loading was presented. Both produce significantly higher AE sig-
879 nals compared to any other crack front related AE activity, while
880 their particular fracture surface pattern evidenced local velocities
881 around $30\text{-}200\text{ m}\cdot\text{s}^{-1}$ (see (?)).
- 882 • A linear relationship between AE absolute energy of HA signals
883 and the log of the fracture growth area has been found considering
884 both: the present localized dynamic instabilities and macroscopic
885 stick-slip phenomenon investigated in the previous work (see (?)).
886 An attempt of extrapolation, from this relationship to LA signals,
887 has been done leading to potential fracture growth area of about
888 $150 \times 150\ \mu\text{m}$. It may evidence that LA emission are rather induced
889 by localized small crack growth than macroscopic crack advance.
- 890 • Two important multiplets have been observed composed of 15 and
891 8 successive AE signals with highly correlated impulsive waveform
892 parts. While their impulsive parts clearly characterize them, it has
893 been found difficult to find a similar classification using standard
894 procedures such as k-means or DBSCAN clustering algorithms of
895 the waveforms in the dominant PC space of the AE descriptors. In-
896 deed most of the LA signals share close characteristics, and consid-
897 ering the entire wave form instead of only the impulsive part makes
898 classification difficult.
- 899 • No clear relationship between post-mortem fracture surface fea-
900 tures, transient crack front kinematics and multiplets, or system-

901 atical identification of source mechanisms has been found, which
902 reflects the complexity of classifying (especially in a blind NDT ap-
903 proach) AE signals sharing similar AE amplitudes. A proposition
904 has been done, linking AE to localized crack front accelerations
905 in line with the HA signal analysis and AE/velocity heterogeneity
906 observations done macroscopically. However, conclusions remain
907 vague.

908 This paper has demonstrated that combining different investigation tools
909 – surface and in-volume imagine, AE and post-mortem analysis – AE sources
910 and the crack front can be undoubtedly connected for AE signals with extreme
911 characteristics such as dynamic instabilities. However, classification of LA sig-
912 nals, dominant during quasi-static crack propagation, remains highly difficult
913 to connect unambiguously to a particular source mechanism even for highly
914 correlated waveforms successively reappearing along 15 mm of crack propa-
915 gation. We do believe that such lab experiment may help the design of NDT
916 algorithm discriminating in-real time different AE sources. Nevertheless, to
917 completely shed light on all blind-spots in the process of AE source identifica-
918 tion, one would need to account for the visualization of elastic waves traveling
919 from their source to the transducer. Here, the presented experimental cam-
920 paign would need to be extended by an ultra-high speed imaging device with
921 potential high spatial resolution (Vinel et al., 2021). However, with expected
922 strain levels induced by the energy released during small crack propagation,
923 this remains a significant experimental challenge.

924 **Acknowledgement**

925 The authors gratefully acknowledge the support of the Agence Nationale de
926 la Recherche (ANR) through grant ANR-19-CE42-0012.

927 **Declarations**

928 *Conflict of interest:*

929 No conflict of interest is declared by the authors.

930 **Appendix A. Fracture parameters by DIC**

931 The foundation for retrieving the sought-after fracture mechanics variables
932 is found in DIC by providing fullfield displacement measurements from se-
933 quential images. By following the principle of conservation of brightness be-
934 tween a reference (f) and a deformed image (g), i.e. the equation of optical

935 flow, DIC presents an ill-posed non-linear inverse problem:

$$f(\underline{X}) = g(\underline{X} + \underline{u}(\underline{X})) \quad (\text{A.1})$$

936 with $\underline{u}(\underline{X})$ being the sought displacement field. To bypass this ill-posed prob-
 937 lem, the pixel displacement has to be parameterized using shape functions.
 938 Here, FE discretization has been used (Besnard et al., 2006). Eventually, the
 939 problem can be linearized and solved iteratively in a least-squares sense. A
 940 median regularization is used to mitigate detrimental impact of noise and
 941 smaller elements. By post-treating the displacement field, variables relevant
 942 for fracture mechanics analysis (e.g. SIFs and crack tip positions) were derived
 943 through Williams' series expansion. Traditionally, in the case of a semi infinite
 944 linear elastic isotropic media, stress and displacement fields around the crack
 945 tip depend on SIF, the distance to the crack tip (r) and the angle (θ) in a polar
 946 reference system attached to the crack tip (Williams, 1957). Thus, by knowing
 947 the displacement field through DIC and projecting it onto the analytical solu-
 948 tion, different fracture mechanics parameters can be derived through a non-
 949 linear inverse problem (Roux and Hild, 2006; Réthoré, 2015; Roux-Langlois
 950 et al., 2015). The displacement field around the crack tip is written as following:

$$u(r, \theta) = \sum_{i=I, II} \sum_{n=-\infty}^{\infty} A_i^n r^{n/2} g_i^n(\theta) \quad (\text{A.2})$$

951 with the distance to the crack tip r , the angle θ in a polar reference system
 952 attached to the crack tip, Williams' coefficients A and base function g . The
 953 base function $g_i^n(\theta)$ has the following form:

$$g_I^n(\theta) = \frac{1}{2\mu} \left[\begin{array}{l} (\kappa + n/2 + (-1)^n) \cos[(n/2)\theta] - (n/2) \cos[(n/2 - 2)\theta] \\ (\kappa - n/2 - (-1)^n) \sin[(n/2)\theta] + (n/2) \sin[(n/2 - 2)\theta] \end{array} \right]_{(e_t, e_n)} \quad (\text{A.3})$$

$$g_{II}^n(\theta) = \frac{1}{2\mu} \left[\begin{array}{l} -(\kappa + n/2 - (-1)^n) \sin[(n/2)\theta] + (n/2) \sin[(n/2 - 2)\theta] \\ (\kappa - n/2 - (-1)^n) \cos[(n/2)\theta] + (n/2) \cos[(n/2 - 2)\theta] \end{array} \right]_{(e_t, e_n)} \quad (\text{A.4})$$

954 with μ and κ being the shear modulus and the Kolosov's constant, respectively.
 955 Kolosov's constant under plane stress is $\kappa = (3 - \nu)/(1 + \nu)$ with ν being the
 956 Poisson's ratio.

957 Equation A.2 states, that displacements can be computed for an infinite
 958 sum of modes. However, limiting the solution to $n_{min} = -3$ and $n_{max} = 7$
 959 is sufficient to retain the relevant crack features. For quasi-brittle medium, good
 960 agreement of the mechanical fields can be established outside the process zone
 961 of the crack for the following Williams' series coefficient (A_i^n) solutions:

962 $n = 0$, in-plane rigid body translations

963 $n = 1$, asymptotic terms K_I and K_{II}

964 $n = 2$, T-stress and in-plane body rotations

965 Notice that the projection zone (Figure 6) is defined by R_{min} and R_{max} . On
966 the one hand, the asymptotic behaviour near the crack tip of the fields com-
967 puted by the super-singular terms ($n < 0$) do not provide any physical meaning
968 and are therefore classically neglected. However, when the crack tip position is
969 sought, these super-singular functions appear in the required basis ($n = -1$ be-
970 ing, up to a scaling factor, the derivative of $n = 1$ with respect to the assumed
971 crack tip position). To not induce biases due to truncation, terms for n down
972 to -3 are considered. Hence, data at a distance to the crack tip smaller than
973 R_{min} are discarded to maintain reasonable conditioning of the least-squares
974 problem. On the other hand, R_{max} – defining the projection zone size exter-
975 nally – has to be small enough to avoid influences of the free boundary, but
976 large enough to still include a sufficient amount of mesh points in the domain.
977 The right size of projection zone, i.e. defining R_{min} and R_{max} (see Table 3),
978 has been identified through a parametric study. Furthermore, by using a pre-
979 defined crack path, the super-singular term $n = -1$ is used to estimate the po-
980 sition to the equivalent elastic crack tip along this path (Réthoré et al., 2011).

981 **Appendix B. Principle component analysis**

982 In AE analysis, 16 AE waveform parameters are computed by the AE system.
983 They are used as waveform descriptors to define the characteristics of each AE
984 hit. The descriptors are defined as following:

- 985 • Amplitude - highest voltage in the AE waveform, expressed on the dB AE
986 amplitude scale.
- 987 • Energy - time integral of the absolute signal voltage. The reported mag-
988 nitude, depends on the value selected for Energy Reference Gain. Pro-
989 portional to Signal Strength.
- 990 • Counts - number of times the signal crosses the detection threshold.
- 991 • Duration - time from first to last threshold crossing (μ s).
- 992 • RMS - root mean square voltage during a period of time based on a soft-
993 ware programmable time constant, referred to the input to the signal
994 processing board.

- 995 • ASL - RMS, converted to the dB AE scale (0dB AE = 1 μ V at the sensor,
996 before any amplification).
- 997 • Threshold - detection threshold, on the dB AE scale.
- 998 • Rise Time - time from first threshold crossing to highest voltage point on
999 the waveform (μ s).
- 1000 • Counts to Peak - number of threshold crossings from first to highest volt-
1001 age point on the waveform.
- 1002 • Average Frequency - Counts divided by Duration, divided by 1000 (thus,
1003 kHz). Note that this is not a spectral domain calculation, but a calcula-
1004 tion from time domain features.
- 1005 • Reverberation Frequency - (Counts - Counts to Peak) divided by (Dura-
1006 tion - Risetime). .
- 1007 • Initiation Frequency - Counts to Peak divided by Risetime.
- 1008 • Signal Strength - time integral of the absolute signal voltage, expressed
1009 in pVs (picovolt-seconds) referenced to the sensor, before any amplifica-
1010 tion. Proportional to Energy.
- 1011 • Absolute Energy - time integral of the square of the signal voltage at the
1012 sensor before any amplification, divided by a 10k Ω impedance and ex-
1013 pressed in aJ (attojoules).
- 1014 • Frequency centroid - the center of mass of the power spectrum graph.
- 1015 • Peak frequency - the point where the power spectrum is greatest.

1016 These descriptors are being used to identify similarities among different AE re-
1017 sponses and thereby help linking them to physical, chemical and/or mechani-
1018 cal source mechanisms. In literature and industry, different methods are being
1019 used to distinguish among sets of AE responses. Here, the Mistras group soft-
1020 ware Noesis has been taken as reference and replicated in Matlab. The follow-
1021 ing methodology has then been pursued, presented on example data:

- 1022 1. *Correlation matrix of waveform descriptors*
1023 Here, a Pearson (Freedman, David et al., 2007) pairwise linear correla-
1024 tion between each pair of columns, i.e. waveform descriptors, has been

1025 performed as followed:

$$\rho(a, b) = \frac{\sum_{i=1}^n (X_{a,i} - \bar{X}_a)(X_{b,i} - \bar{X}_b)}{[\sum_{i=1}^n (X_{a,i} - \bar{X}_a)^2 \sum_{j=1}^n (X_{b,j} - \bar{X}_b)^2]^{1/2}}, \quad (\text{B.1})$$

1026 with

$$\bar{X}_a = \frac{\sum_{i=1}^n X_{a,i}}{n} \quad (\text{B.2})$$

1027 and

$$\bar{X}_b = \frac{\sum_{j=1}^n X_{b,j}}{n}, \quad (\text{B.3})$$

1028 where X_a and X_b are columns in the parametric matrix, while n is the
1029 length of the column.

1030 2. *Dendrogram plot of correlation matrix*

1031 The degree of correlation between the features of the data set has then
1032 been displayed in the form of a dendrogram. With the most correlated
1033 features joined together at the top, the degree of correlation decreases
1034 towards the bottom of the graph. This has been done to narrow down
1035 the amount of descriptors to be used for clustering and hence neglect
1036 descriptors with similar tendencies. The dendrogram plot is presented in
1037 Figure B.23. Descriptors that have high coefficients of correlation (again,
1038 1.0 being the maximum) are linked at their value of correlation and can
1039 thereby be identified.

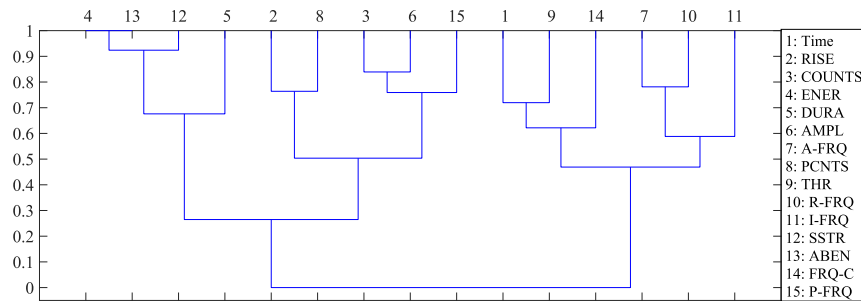


Figure B.23: Correlation matrix of waveform descriptors presented as dendrogram.

1040 In this example, very strong correlation is found between Energy and
1041 Absolute Energy, which would allow the user to neglect one of them to
1042 reduce complexity without losing information. Remaining parameters
1043 are then used for the continuation of the analysis.

1044 3. *Principle components analysis*

1045 The principle component analysis (Karamizadeh et al., 2013) has been
1046 applied to increase understanding of the AE observation. In a first step,
1047 the most relevant principle components have to be identified.

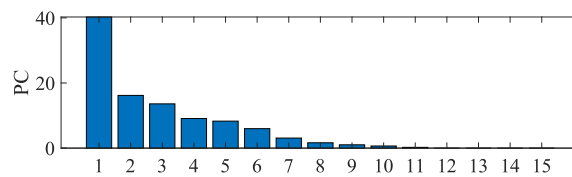


Figure B.24: Evaluation of most influential principle component axes.

1048 Based on the example case of a typical PCA of waveform descriptors pre-
1049 sented in Figure B.24, the first and second principle components con-
1050 tribute the most to the differentiation of the waveforms. Thus, investi-
1051 gated data would best be visualized in the space of the two axis. Their
1052 contribution by each AE parameter is presented in Figure B.25.

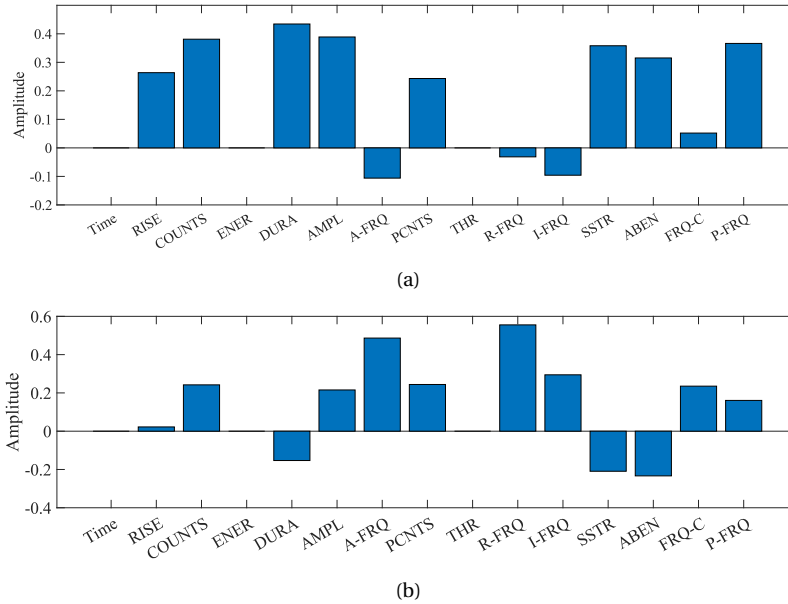
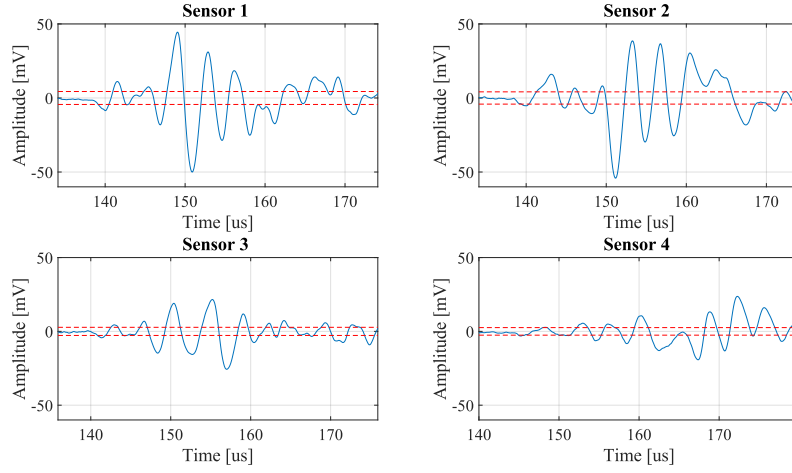


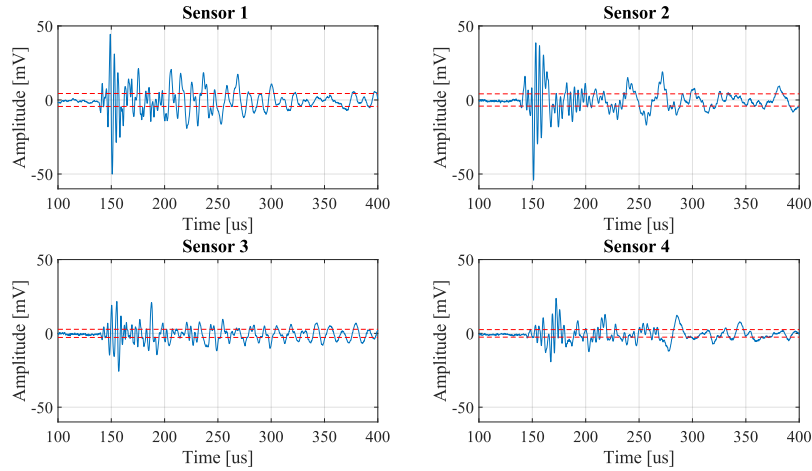
Figure B.25: Feature contributions to the (a) first and (b) second principle component axis.

1053 Appendix C. Sensor comparison

1054 This appendix presents a particular AE signal – extracted from a multiplet
 1055 – received at all four sensors. Figure C.26 shows the same signal detected at all
 1056 four sensors for (a) $300 \mu\text{s}$ and (b) $40 \mu\text{s}$ (impulsive) of the entire signal dura-
 1057 tion. The threshold is indicated by the red dashed lines. AE parameters of the
 1058 signal computed for all four sensors are presented in Figure C.6. Figure C.26(b)
 1059 corresponds to a signal being presented in the core of paper in Figure 19 asso-
 1060 ciated to Multiplet 1.



(a)



(b)

Figure C.26: Same signal detected at all four sensors for (a) $300 \mu\text{s}$ and (b) $40 \mu\text{s}$ (coda) of the signal. The threshold is indicated by the red dashed lines.

Table C.6: AE parameters computed for the signal in Figure C.26 in chronological order of the sensor number.

Time	RISE	COUN	ENER	DURA	AMP	A-FRQ	PCNTS	THR	R-FRQ	I-FRQ	SIG STR	ABS-ENER	FRQ-C	P-FRQ
2.4769143	12	27	3	975	53	28	3	31	25	250	2606.29	19.72	1904	106
2.4769145	12	31	2	975	52	32	3	31	29	250	2169.2	17.21	1449	41
2.4769161	17	32	2	973	47	33	4	31	29	235	1773.92	8.07	1276	93
2.4769203	28	27	2	969	48	28	6	31	22	214	1795.97	7.3	1667	1

1061 As precised in the core of the text, we can observe that the same source
1062 event can produce a significantly different signal on each sensors. While all
1063 the analysis in the paper has been done on Sensor 2, it shows that performing
1064 the analysis on different sensor may lead to slightly different results in term of
1065 classification and multiplet detection. In the present case, Sensor 1 and Sen-
1066 sor 2 are systematically behind the crack front, while Sensor 3 and Sensor 4 are
1067 in front. We observe that the main difference, in terms of impulsive response
1068 (see Figure C.26(b)), is observed between signals in front or behind the source,
1069 which potentially evidences a clear directionality of the wave propagating. It
1070 underlines the complexity of analysis and classifying, in a bulk, crack propa-
1071 gating, branching, turning with respect to the sensors.

1072 **References**

- 1073 Abel, J., Smith, J., 1987. The spherical interpolation method for closed-
1074 form passive source localization using range difference measurements, in:
1075 ICASSP '87. IEEE International Conference on Acoustics, Speech, and Sig-
1076 nal Processing, Institute of Electrical and Electronics Engineers, Dallas,
1077 TX, USA. pp. 471–474. URL: [http://ieeexplore.ieee.org/document/](http://ieeexplore.ieee.org/document/1169674/)
1078 [1169674/](http://ieeexplore.ieee.org/document/1169674/), doi:10.1109/ICASSP.1987.1169674.
- 1079 Aggelis, D.G., 2011. Classification of cracking mode in concrete by acous-
1080 tic emission parameters. *Mechanics Research Communications* 38,
1081 153–157. URL: [https://linkinghub.elsevier.com/retrieve/pii/](https://linkinghub.elsevier.com/retrieve/pii/S0093641311000620)
1082 [S0093641311000620](https://linkinghub.elsevier.com/retrieve/pii/S0093641311000620), doi:10.1016/j.mechrescom.2011.03.007.
- 1083 Almeida, R.S., Magalhães, M.D., Karim, M.N., Tushtev, K., Rezwan, K.,
1084 2023. Identifying damage mechanisms of composites by acoustic
1085 emission and supervised machine learning. *Materials & Design* 227,
1086 111745. URL: [https://linkinghub.elsevier.com/retrieve/pii/](https://linkinghub.elsevier.com/retrieve/pii/S0264127523001600)
1087 [S0264127523001600](https://linkinghub.elsevier.com/retrieve/pii/S0264127523001600), doi:10.1016/j.matdes.2023.111745.
- 1088 Andraju, L.B., Raju, G., 2023. Damage characterization of CFRP lami-
1089 nates using acoustic emission and digital image correlation: Clustering,
1090 damage identification and classification. *Engineering Fracture Mechan-*
1091 *ics* 277, 108993. URL: [https://www.sciencedirect.com/science/](https://www.sciencedirect.com/science/article/pii/S0013794422007160)
1092 [article/pii/S0013794422007160](https://www.sciencedirect.com/science/article/pii/S0013794422007160), doi:[https://doi.org/10.1016/](https://doi.org/10.1016/j.engfracmech.2022.108993)
1093 [j.engfracmech.2022.108993](https://doi.org/10.1016/j.engfracmech.2022.108993).
- 1094 Arnau, A., Soares, D., 2008. Fundamentals of Piezoelectricity, in: Vives, A.A.
1095 (Ed.), *Piezoelectric Transducers and Applications*. Springer Berlin Heidel-
1096 berg, Berlin, Heidelberg, pp. 1–38. URL: <http://link.springer.com/>

- 1097 10.1007/978-3-540-77508-9_1, doi:10.1007/978-3-540-77508-9_
1098 1.
- 1099 Arumugam, V., Barath Kumar, S., Joseph Stanley, A., 2011. Effect of fuzzy C
1100 means technique in failure mode discrimination of glass/epoxy laminates
1101 using acoustic emission monitoring. *Russ J Nondestruct Test* 47, 858–864.
1102 URL: <http://link.springer.com/10.1134/S1061830911120035>,
1103 doi:10.1134/S1061830911120035.
- 1104 Besnard, G., Hild, F., Roux, S., 2006. “Finite-Element” Displacement Fields
1105 Analysis from Digital Images: Application to Portevin–Le Châtelier Bands.
1106 *Exp Mech* 46, 789–803. URL: [http://link.springer.com/10.1007/
1107 s11340-006-9824-8](http://link.springer.com/10.1007/s11340-006-9824-8), doi:10.1007/s11340-006-9824-8.
- 1108 Bonamy, D., Ravi-Chandar, K., 2003. Interaction of Shear Waves and Propagat-
1109 ing Cracks. *Phys. Rev. Lett.* 91, 235502. URL: [https://link.aps.org/
1110 doi/10.1103/PhysRevLett.91.235502](https://link.aps.org/doi/10.1103/PhysRevLett.91.235502), doi:10.1103/PhysRevLett.
1111 91.235502.
- 1112 Cao, Z., Wang, B.F., Wang, K.M., Lin, H.G., Yu, R.Q., 1998. Chemical acous-
1113 tic emissions from gas evolution processes recorded by a piezoelectric
1114 transducer. *Sensors and Actuators B: Chemical* 50, 27–37. URL: [https:
1115 //linkinghub.elsevier.com/retrieve/pii/S092540059800152X](https://linkinghub.elsevier.com/retrieve/pii/S092540059800152X),
1116 doi:10.1016/S0925-4005(98)00152-X.
- 1117 Cheng, L., Xin, H., Groves, R.M., Veljkovic, M., 2021. Acoustic emission source
1118 location using Lamb wave propagation simulation and artificial neural net-
1119 work for I-shaped steel girder. *Construction and Building Materials* 273,
1120 121706. URL: [https://linkinghub.elsevier.com/retrieve/pii/
1121 S0950061820337107](https://linkinghub.elsevier.com/retrieve/pii/S0950061820337107), doi:10.1016/j.conbuildmat.2020.121706.
- 1122 Ciaburro, G., Iannace, G., 2022. Machine-Learning-Based Methods
1123 for Acoustic Emission Testing: A Review. *Applied Sciences* 12,
1124 10476. URL: <https://www.mdpi.com/2076-3417/12/20/10476>,
1125 doi:10.3390/app122010476.
- 1126 Ciampa, F., Meo, M., 2010. A new algorithm for acoustic emission lo-
1127 calization and flexural group velocity determination in anisotropic struc-
1128 tures. *Composites Part A: Applied Science and Manufacturing* 41, 1777–
1129 1786. URL: [https://linkinghub.elsevier.com/retrieve/pii/
1130 S1359835X10002332](https://linkinghub.elsevier.com/retrieve/pii/S1359835X10002332), doi:10.1016/j.compositesa.2010.08.013.

- 1131 Crandall, D., Moore, J., Gill, M., Stadelman, M., 2017. CT scan-
1132 ning and flow measurements of shale fractures after multiple shearing
1133 events. *International Journal of Rock Mechanics and Mining Sciences* 100,
1134 177–187. URL: [https://linkinghub.elsevier.com/retrieve/pii/
1135 S136516091630449X](https://linkinghub.elsevier.com/retrieve/pii/S136516091630449X), doi:10.1016/j.ijrmms.2017.10.016.
- 1136 Dehghan Niri, E., Salamone, S., 2012. A probabilistic framework for acoustic
1137 emission source localization in plate-like structures. *Smart Mater. Struct.*
1138 21, 035009. URL: [https://iopscience.iop.org/article/10.1088/
1139 0964-1726/21/3/035009](https://iopscience.iop.org/article/10.1088/0964-1726/21/3/035009), doi:10.1088/0964-1726/21/3/035009.
- 1140 Deschanel, S., Ben Rhouma, W., Weiss, J., 2017. Acoustic emission multiplets
1141 as early warnings of fatigue failure in metallic materials. *Sci Rep* 7, 13680.
1142 URL: <http://www.nature.com/articles/s41598-017-13226-1>,
1143 doi:10.1038/s41598-017-13226-1.
- 1144 Dong, L., Zou, W., Sun, D., Tong, X., Li, X., Shu, W., 2019. Some Develop-
1145 ments and New Insights for Microseismic/Acoustic Emission Source Local-
1146 ization. *Shock and Vibration* 2019, 1–15. URL: [https://www.hindawi.
1147 com/journals/sv/2019/9732606/](https://www.hindawi.com/journals/sv/2019/9732606/), doi:10.1155/2019/9732606.
- 1148 Freedman, David, Pisani, Robert, Purves, Roger, Adhikari, Ani, 2007. *Statistics*.
1149 WW Norton & Company New York .
- 1150 Gonzalez, R.C., Eddins, S.L., Woods, R.E., 2004. *Digital image publishing using*
1151 *MATLAB*. Prentice Hall.
- 1152 Grosse, C., Ohtsu, M. (Eds.), 2008. *Acoustic Emission Testing*. Springer Berlin
1153 Heidelberg, Berlin, Heidelberg. URL: [http://link.springer.com/10.
1154 1007/978-3-540-69972-9](http://link.springer.com/10.1007/978-3-540-69972-9), doi:10.1007/978-3-540-69972-9.
- 1155 Gul, S., Tabrizi, I.E., Okan, B.S., Kefal, A., Yildiz, M., 2021. An experimen-
1156 tal investigation on damage mechanisms of thick hybrid composite
1157 structures under flexural loading using multi-instrument measurements.
1158 *Aerospace Science and Technology* 117, 106921. URL: [https://www.
1159 sciencedirect.com/science/article/pii/S1270963821004314](https://www.sciencedirect.com/science/article/pii/S1270963821004314),
1160 doi:<https://doi.org/10.1016/j.ast.2021.106921>.
- 1161 Guo, M., Alam, S.Y., Bendimerad, A.Z., Grondin, F., Rozière, E., Loukili, A.,
1162 2017. Fracture process zone characteristics and identification of the micro-
1163 fracture phases in recycled concrete. *Engineering Fracture Mechanics* 181,
1164 101–115. URL: [https://linkinghub.elsevier.com/retrieve/pii/
1165 S001379441730406X](https://linkinghub.elsevier.com/retrieve/pii/S001379441730406X), doi:10.1016/j.engfracmech.2017.07.004.

- 1166 Guo, Y., Shang, D., Zuo, L., Qu, L., Hou, G., Cai, D., Jin, T., Yin, X., 2022. Identifi-
1167 cation of fatigue damage modes for carbon fiber/epoxy composites using
1168 acoustic emission monitoring under fully reversed loading. *Polymer Com-*
1169 *posites* 43, 3371–3385. URL: [https://onlinelibrary.wiley.com/doi/](https://onlinelibrary.wiley.com/doi/10.1002/pc.26622)
1170 [10.1002/pc.26622](https://onlinelibrary.wiley.com/doi/10.1002/pc.26622), doi:10.1002/pc.26622.
- 1171 Hamam, R., Hild, F., Roux, S., 2007. Stress Intensity Factor Gauging
1172 by Digital Image Correlation: Application in Cyclic Fatigue. *Strain* 43,
1173 181–192. URL: [https://onlinelibrary.wiley.com/doi/10.1111/j.](https://onlinelibrary.wiley.com/doi/10.1111/j.1475-1305.2007.00345.x)
1174 [1475-1305.2007.00345.x](https://onlinelibrary.wiley.com/doi/10.1111/j.1475-1305.2007.00345.x), doi:10.1111/j.1475-1305.2007.00345.
1175 x.
- 1176 Hassan, F., Mahmood, A.K.B., Yahya, N., Saboor, A., Abbas, M.Z., Khan,
1177 Z., Rimsan, M., 2021. State-of-the-Art Review on the Acoustic Emission
1178 Source Localization Techniques. *IEEE Access* 9, 101246–101266. URL:
1179 <https://ieeexplore.ieee.org/document/9481912/>, doi:10.1109/
1180 ACCESS.2021.3096930.
- 1181 Hattali, M., Barés, J., Ponson, L., Bonamy, D., 2012. Low Velocity Surface Frac-
1182 ture Patterns in Brittle Material: A Newly Evidenced Mechanical Instabil-
1183 ity. *MSF* 706-709, 920–924. URL: [https://www.scientific.net/MSF.](https://www.scientific.net/MSF.706-709.920)
1184 [706-709.920](https://www.scientific.net/MSF.706-709.920), doi:10.4028/www.scientific.net/MSF.706-709.920.
- 1185 Heinzmann, R., Seghir, R., Alam, S.Y., Réthoré, J., 2023. Experimental investiga-
1186 tion of the alternate recurrence of quasi-static and dynamic crack propaga-
1187 tion in PMMA. *Int J Fract* URL: [https://link.springer.com/10.1007/](https://link.springer.com/10.1007/s10704-023-00717-8)
1188 [s10704-023-00717-8](https://link.springer.com/10.1007/s10704-023-00717-8), doi:10.1007/s10704-023-00717-8.
- 1189 Henninger, C., Roux, S., Hild, F., 2010. Enriched kinematic fields of
1190 cracked structures. *International Journal of Solids and Structures* 47,
1191 3305–3316. URL: [https://linkinghub.elsevier.com/retrieve/](https://linkinghub.elsevier.com/retrieve/pii/S002076831000291X)
1192 [pii/S002076831000291X](https://linkinghub.elsevier.com/retrieve/pii/S002076831000291X), doi:10.1016/j.ijsolstr.2010.08.012.
- 1193 Hensman, J., Mills, R., Pierce, S., Worden, K., Eaton, M., 2010. Locating
1194 acoustic emission sources in complex structures using Gaussian processes.
1195 *Mechanical Systems and Signal Processing* 24, 211–223. URL: [https:](https://linkinghub.elsevier.com/retrieve/pii/S0888327009001885)
1196 [//linkinghub.elsevier.com/retrieve/pii/S0888327009001885](https://linkinghub.elsevier.com/retrieve/pii/S0888327009001885),
1197 doi:10.1016/j.ymsp.2009.05.018.
- 1198 Jayakumar, T., Mukhopadhyay, C., Venugopal, S., Mannan, S., Raj, B., 2005. A
1199 review of the application of acoustic emission techniques for monitoring

- 1200 forming and grinding processes. *Journal of Materials Processing Technol-*
1201 *ogy* 159, 48–61. URL: [https://linkinghub.elsevier.com/retrieve/](https://linkinghub.elsevier.com/retrieve/pii/S0924013604000615)
1202 [pii/S0924013604000615](https://linkinghub.elsevier.com/retrieve/pii/S0924013604000615), doi:10.1016/j.jmatprotec.2004.01.034.
- 1203 Karamizadeh, S., Abdullah, S.M., Manaf, A.A., Zamani, M., Hooman, A.,
1204 2013. An Overview of Principal Component Analysis. *JSIP* 04, 173–
1205 175. URL: [http://www.scirp.org/journal/doi.aspx?DOI=10.4236/](http://www.scirp.org/journal/doi.aspx?DOI=10.4236/jsip.2013.43B031)
1206 [jsip.2013.43B031](http://www.scirp.org/journal/doi.aspx?DOI=10.4236/jsip.2013.43B031), doi:10.4236/jsip.2013.43B031.
- 1207 Kong, Y., Bennett, C., Hyde, C., 2020. A review of non-destructive
1208 testing techniques for the in-situ investigation of fretting fa-
1209 tigue cracks. *Materials & Design* 196, 109093. URL: <https://linkinghub.elsevier.com/retrieve/pii/S0264127520306286>,
1210 [doi:10.1016/j.matdes.2020.109093](https://linkinghub.elsevier.com/retrieve/pii/S0264127520306286).
1211
- 1212 Li, L., Lomov, S.V., Yan, X., Carvelli, V., 2014. Cluster analysis of
1213 acoustic emission signals for 2D and 3D woven glass/epoxy compos-
1214 ites. *Composite Structures* 116, 286–299. URL: [https://linkinghub.](https://linkinghub.elsevier.com/retrieve/pii/S0263822314002335)
1215 [elsevier.com/retrieve/pii/S0263822314002335](https://linkinghub.elsevier.com/retrieve/pii/S0263822314002335), doi:10.1016/j.
1216 [compstruct.2014.05.023](https://linkinghub.elsevier.com/retrieve/pii/S0263822314002335).
- 1217 Maillet, E., Baker, C., Morscher, G.N., Pujar, V.V., Lemanski, J.R., 2015. Feasi-
1218 bility and limitations of damage identification in composite materials using
1219 acoustic emission. *Composites Part A: Applied Science and Manufacturing*
1220 75, 77–83. URL: [https://linkinghub.elsevier.com/retrieve/pii/](https://linkinghub.elsevier.com/retrieve/pii/S1359835X15001499)
1221 [S1359835X15001499](https://linkinghub.elsevier.com/retrieve/pii/S1359835X15001499), doi:10.1016/j.compositesa.2015.05.003.
- 1222 Noorsuhada, M.N., Abdul Hakeem, Z., Soffian Noor, M.S., Noor Syafeekha,
1223 M.S., Azmi, I., 2017. Correlation between average frequency and RA value
1224 (rise time/amplitude) for crack classification of reinforced concrete beam
1225 using acoustic emission technique, Langkawi, Malaysia. p. 050001. URL:
1226 <https://pubs.aip.org/aip/acp/article/886503>, doi:10.1063/1.
1227 [5010497](https://pubs.aip.org/aip/acp/article/886503).
- 1228 Ravi-Chandar, K., Balzano, M., 1988. On the mechanics and mechanisms of
1229 crack growth in polymeric materials. *Engineering Fracture Mechanics* 30,
1230 713–727. URL: [https://linkinghub.elsevier.com/retrieve/pii/](https://linkinghub.elsevier.com/retrieve/pii/0013794488901610)
1231 [0013794488901610](https://linkinghub.elsevier.com/retrieve/pii/0013794488901610), doi:10.1016/0013-7944(88)90161-0.
- 1232 Romhány, G., Czigány, T., Karger-Kocsis, J., 2017. Failure Assessment and Eval-
1233 uation of Damage Development and Crack Growth in Polymer Composites
1234 Via Localization of Acoustic Emission Events: A Review. *Polymer Reviews* 57,

- 1235 397–439. URL: [https://www.tandfonline.com/doi/full/10.1080/](https://www.tandfonline.com/doi/full/10.1080/15583724.2017.1309663)
1236 15583724.2017.1309663, doi:10.1080/15583724.2017.1309663.
- 1237 Roux, S., Hild, F., 2006. Stress intensity factor measurements from digi-
1238 tal image correlation: post-processing and integrated approaches. *Int*
1239 *J Fract* 140, 141–157. URL: [http://link.springer.com/10.1007/](http://link.springer.com/10.1007/s10704-006-6631-2)
1240 [s10704-006-6631-2](http://link.springer.com/10.1007/s10704-006-6631-2), doi:10.1007/s10704-006-6631-2.
- 1241 Roux, S., Réthoré, J., Hild, F., 2009. Digital image correlation and
1242 fracture: an advanced technique for estimating stress intensity fac-
1243 tors of 2D and 3D cracks. *J. Phys. D: Appl. Phys.* 42, 214004.
1244 URL: [https://iopscience.iop.org/article/10.1088/0022-3727/](https://iopscience.iop.org/article/10.1088/0022-3727/42/21/214004)
1245 [42/21/214004](https://iopscience.iop.org/article/10.1088/0022-3727/42/21/214004), doi:10.1088/0022-3727/42/21/214004.
- 1246 Roux-Langlois, C., Gravouil, A., Baietto, M.C., Réthoré, J., Mathieu, F., Hild,
1247 F., Roux, S., 2015. DIC identification and X-FEM simulation of fatigue
1248 crack growth based on the Williams’ series. *International Journal of*
1249 *Solids and Structures* 53, 38–47. URL: [https://linkinghub.elsevier.](https://linkinghub.elsevier.com/retrieve/pii/S0020768314004053)
1250 [com/retrieve/pii/S0020768314004053](https://linkinghub.elsevier.com/retrieve/pii/S0020768314004053), doi:10.1016/j.ijsolstr.
1251 2014.10.026.
- 1252 Réthoré, J., 2015. Automatic crack tip detection and stress intensity factors esti-
1253 mation of curved cracks from digital images: Automatic crack tip detection
1254 and SIF estimation of curved cracks. *Int. J. Numer. Meth. Engng* 103, 516–
1255 534. URL: [https://onlinelibrary.wiley.com/doi/10.1002/nme.](https://onlinelibrary.wiley.com/doi/10.1002/nme.4905)
1256 [4905](https://onlinelibrary.wiley.com/doi/10.1002/nme.4905), doi:10.1002/nme.4905.
- 1257 Réthoré, J., 2018. UFreckles. URL: <https://zenodo.org/record/1433776>,
1258 doi:10.5281/ZENODO.1433776. language: en.
- 1259 Réthoré, J., Estevez, R., 2013. Identification of a cohesive zone model from
1260 digital images at the micron-scale. *Journal of the Mechanics and Physics*
1261 *of Solids* 61, 1407–1420. URL: [https://linkinghub.elsevier.com/](https://linkinghub.elsevier.com/retrieve/pii/S0022509613000288)
1262 [retrieve/pii/S0022509613000288](https://linkinghub.elsevier.com/retrieve/pii/S0022509613000288), doi:10.1016/j.jmps.2013.01.
1263 011.
- 1264 Réthoré, J., Roux, S., Hild, F., 2011. Optimal and noise-robust extraction
1265 of Fracture Mechanics parameters from kinematic measurements. *Engi-*
1266 *neering Fracture Mechanics* 78, 1827–1845. URL: [https://linkinghub.](https://linkinghub.elsevier.com/retrieve/pii/S0013794411000312)
1267 [elsevier.com/retrieve/pii/S0013794411000312](https://linkinghub.elsevier.com/retrieve/pii/S0013794411000312), doi:10.1016/j.
1268 [engfracmech](https://linkinghub.elsevier.com/retrieve/pii/S0013794411000312).2011.01.012.

- 1269 Sagar, R.V., Prasad, B.R., Kumar, S.S., 2012. An experimental study on
1270 cracking evolution in concrete and cement mortar by the b-value anal-
1271 ysis of acoustic emission technique. *Cement and Concrete Research*
1272 42, 1094–1104. URL: [https://linkinghub.elsevier.com/retrieve/
1273 pii/S0008884612000981](https://linkinghub.elsevier.com/retrieve/pii/S0008884612000981), doi:10.1016/j.cemconres.2012.05.003.
- 1274 Schau, H., Robinson, A., 1987. Passive source localization employing intersect-
1275 ing spherical surfaces from time-of-arrival differences. *IEEE Trans. Acoust.,
1276 Speech, Signal Process.* 35, 1223–1225. URL: [http://ieeexplore.ieee.
1277 org/document/1165266/](http://ieeexplore.ieee.org/document/1165266/), doi:10.1109/TASSP.1987.1165266.
- 1278 Schmidt, R.O., 1972. A New Approach to Geometry of Range Dif-
1279 ference Location. *IEEE Trans. Aerosp. Electron. Syst.* AES-8, 821–
1280 835. URL: <http://ieeexplore.ieee.org/document/4103057/>,
1281 doi:10.1109/TAES.1972.309614.
- 1282 Scruby, C.B., 1987. An introduction to acoustic emission. *J. Phys. E: Sci. In-
1283 strument.* 20, 946–953. URL: [https://iopscience.iop.org/article/10.
1284 1088/0022-3735/20/8/001](https://iopscience.iop.org/article/10.1088/0022-3735/20/8/001), doi:10.1088/0022-3735/20/8/001.
- 1285 Shrama, K., Pullin, R., Clarke, A., Evans, S.L., 2015. Fatigue crack monitor-
1286 ing in mild steel specimens using acoustic emission and digital image
1287 correlation. *Insight* 57, 346–354. URL: [http://openurl.ingenta.
1288 com/content/xref?genre=article&iissn=1354-2575&volume=57&
1289 issue=6&spage=346](http://openurl.ingenta.com/content/xref?genre=article&iissn=1354-2575&volume=57&issue=6&spage=346), doi:10.1784/insi.2015.57.6.346.
- 1290 Sung, D.U., Oh, J.H., Kim, C.G., Hong, C.S., 2000. Impact Monitoring of Smart
1291 Composite Laminates Using Neural Network and Wavelet Analysis. *Journal
1292 of Intelligent Material Systems and Structures* 11, 180–190. URL: [http:
1293 //journals.sagepub.com/doi/10.1106/N5E7-M37Y-3MAR-2KFH](http://journals.sagepub.com/doi/10.1106/N5E7-M37Y-3MAR-2KFH),
1294 doi:10.1106/N5E7-M37Y-3MAR-2KFH.
- 1295 Vasudevan, A.V., 2018. Deciphering triangular fracture patterns in PMMA : how
1296 crack fragments in mixed mode loading. Ph.D. thesis. Sorbonne University.
1297 URL: <https://tel.archives-ouvertes.fr/tel-02180510>.
- 1298 Vincent-Dospital, T., Toussaint, R., Santucci, S., Vanel, L., Bonamy, D., Hat-
1299 tali, L., Cochard, A., Flekkøy, E.G., Måløy, K.J., 2020. How heat controls
1300 fracture: the thermodynamics of creeping and avalanching cracks. *Soft
1301 Matter* 16, 9590–9602. URL: <http://xlink.rsc.org/?DOI=D0SM01062F>,
1302 doi:10.1039/D0SM01062F.

- 1303 Vinel, A., Seghir, R., Berthe, J., Portemont, G., Réthoré, J., 2021. Metrological
1304 assessment of multi-sensor camera technology for spatially-resolved ultra-
1305 high-speed imaging of transient high strain-rate deformation processes.
1306 Strain 57. URL: [https://onlinelibrary.wiley.com/doi/10.1111/](https://onlinelibrary.wiley.com/doi/10.1111/str.12381)
1307 [str.12381](https://onlinelibrary.wiley.com/doi/10.1111/str.12381), doi:10.1111/str.12381.
- 1308 Wadley, H., Mehrabian, R., 1984. Acoustic emission for materials processing:
1309 a review. Materials Science and Engineering 65, 245–263. URL: [https://](https://linkinghub.elsevier.com/retrieve/pii/0025541684900867)
1310 linkinghub.elsevier.com/retrieve/pii/0025541684900867,
1311 doi:10.1016/0025-5416(84)90086-7.
- 1312 Wang, B., Zhong, S., Lee, T.L., Fancey, K.S., Mi, J., 2020. Non-
1313 destructive testing and evaluation of composite materials/structures:
1314 A state-of-the-art review. Advances in Mechanical Engineering 12,
1315 168781402091376. URL: [http://journals.sagepub.com/doi/10.](http://journals.sagepub.com/doi/10.1177/1687814020913761)
1316 [1177/1687814020913761](http://journals.sagepub.com/doi/10.1177/1687814020913761), doi:10.1177/1687814020913761.
- 1317 Williams, M.L., 1957. On the Stress Distribution at the Base
1318 of a Stationary Crack. Journal of Applied Mechanics 24,
1319 109–114. URL: [https://asmedigitalcollection.asme.](https://asmedigitalcollection.asme.org/appliedmechanics/article/24/1/109/1110895/On-the-Stress-Distribution-at-the-Base-of-a)
1320 [org/appliedmechanics/article/24/1/109/1110895/](https://asmedigitalcollection.asme.org/appliedmechanics/article/24/1/109/1110895/On-the-Stress-Distribution-at-the-Base-of-a)
1321 [On-the-Stress-Distribution-at-the-Base-of-a](https://asmedigitalcollection.asme.org/appliedmechanics/article/24/1/109/1110895/On-the-Stress-Distribution-at-the-Base-of-a), doi:10.1115/1.
1322 4011454.
- 1323 Zhou, Z., Lan, R., Rui, Y., Dong, L., Cai, X., 2021. A New Algebraic Solution for
1324 Acoustic Emission Source Localization without Pre-measuring Wave Velocity.
1325 Sensors 21, 459. URL: <https://www.mdpi.com/1424-8220/21/2/459>,
1326 doi:10.3390/s21020459.
- 1327 Zhou, Z., Rui, Y., Zhou, J., Dong, L., Cai, X., 2018. Locating an Acoustic Emission
1328 Source in Multilayered Media Based on the Refraction Path Method. IEEE Ac-
1329 cess 6, 25090–25099. URL: [https://ieeexplore.ieee.org/document/](https://ieeexplore.ieee.org/document/8290682/)
1330 [8290682/](https://ieeexplore.ieee.org/document/8290682/), doi:10.1109/ACCESS.2018.2805384.